

1 **Upper Atmosphere Responses to the 2022 Hunga Tonga-Hunga Ha’apai**

2 **Volcanic Eruption via Acoustic-Gravity Waves and Air-Sea Interaction**

3 Qinzeng Li<sup>1,5</sup>, Jiyao Xu<sup>1,2\*</sup>, Aditya Riadi Gusman<sup>3</sup>, Hanli Liu<sup>4</sup>, Wei Yuan<sup>1,5</sup>, Weijun Liu<sup>1,5</sup>,  
4 Yajun Zhu<sup>1,5</sup>, and Xiao Liu<sup>6</sup>

5

6 1. State Key Laboratory of Space Weather, National Space Science Center, Chinese Academy of Sciences,  
7 Beijing, 100190, China

8 2. School of Astronomy and Space Science, University of Chinese Academy of Science, Beijing,  
9 100049, China

10 3. GNS Science, Lower Hutt, New Zealand

11 4. High Altitude Observatory, National Center for Atmospheric Research, Boulder, Colorado, USA

12 5. Hainan National Field Science Observation and Research Observatory for Space Weather, National Space  
13 Science Center, Chinese Academy of Sciences, Beijing, 100190, China

14 6. School of Mathematics and Information Science, Henan Normal University, Xinxiang, China

15

16 Corresponding author: Jiyao Xu (jyxu@swl.ac.cn)

17 **Abstract**

18 Multi-group of strong atmospheric waves (wave packets #1-#5) over China associated  
19 with the 2022 Hunga Tonga–Hunga Ha’apai (HTHH) volcano eruptions were observed in the  
20 mesopause region using a ground-based airglow imager network. The horizontal phase speed  
21 of wave packet #1 and #2 is approximately 309 m/s and 236 m/s respectively, which is  
22 consistent with Lamb wave L0 mode and L1 mode from theoretical prediction. The amplitude  
23 of the lamb wave L1 mode is larger than that of L0 mode. The wave fronts of Lamb wave L0  
24 and L1 below the lower thermosphere are vertical, while the wave fronts of L0 mode tilt  
25 forward above exhibiting internal wave characteristics, which show good agreement with the  
26 theoretical results. Two types of tsunamis were simulated, one type of tsunami is induced by  
27 the atmospheric pressure wave (TIAPW) and the other type tsunami is directly induced by the  
28 Tonga volcano eruption (TITVE). From backward ray tracing analysis, the TIAPW and  
29 TITVE were likely the sources of the wave packet #3 and wave packets #4-5, respectively.  
30 The scale of tsunamis near the coast is very consistent with the atmospheric AGWs observed  
31 by the airglow network. The AGWs triggered by TITVE propagate nearly 3000 km inland  
32 with the support of duct. The atmospheric pressure wave can directly affect the upper  
33 atmosphere, and can also be coupled with the upper atmosphere through the indirect way of  
34 generating tsunami and subsequently tsunami generating AGWs, which will provide a new  
35 understanding of the coupling between ocean and atmosphere.

## 36 **1. Introduction**

37 Hunga Tonga–Hunga Ha’apai (HTHH) volcano, which erupted at 04:14:45 UT on  
38 January 15, 2022, produced the largest volcanic eruption in terms of energy release of a  
39 single event since the Krakatoa volcanic eruption (Symons, 1888) in 1883. This volcanic  
40 eruption triggered broad spectrum atmospheric disturbances (Adam, 2022; Duncombe,  
41 2022; Wright et al., 2022), including Lamb waves (Zhang et al., 2022), acoustic waves,  
42 gravity waves (GWs) (Liu et al., 2022), and shock waves (Astafyeva et al., 2022). In  
43 addition, the travelling ionospheric disturbances (TIDs) caused by this volcanic eruption  
44 have also been reported (Themens et al., 2022; Lin et al., 2022).

45 Lamb waves are external wave propagating along Earth’s surface at the speed of  
46 sound (Beer, 1974). They are non-dispersive or nearly non-dispersive (Francis, 1973) and  
47 can propagate horizontally over long distances. Lamb wave mainly occupies the  
48 troposphere, and its perturbation pressure decays exponentially with height (Yeh and Liu,  
49 1974). The Lamb waves excited by the Tonga volcano eruptions went around the Earth  
50 several times (Amores et al., 2022; Duncombe, 2022). Sepúlveda et al. (2023) found that  
51 the wind field strongly affects the morphology and propagation of Lamb wave. Liu et al.  
52 (2023) reproduced the Lamb wave L0 and L1 modes consistently with theoretical  
53 predictions (Francis, 1973) using high-resolution Whole Atmosphere Community Climate  
54 Model with thermosphere/ionosphere extension (WACCM-X). Li et al. (2023) identified  
55 Lamb wave L1 mode using phase-leveling amplitude technology based on global  
56 navigation satellite system (GNSS)-total electron content (TEC). Poblet et al. (2023)  
57 reported that the strong perturbations in the meteor radar horizontal wind field over South

58 America is caused by lamb wave L1 mode associated with the 2022 HTHH volcano  
59 eruption.

60 Acoustic-gravity waves (AGWs) are mechanical waves in compressible fluids in a  
61 gravity field (Gossard and Hooke, 1975). If the frequencies are much larger than the  
62 buoyancy frequency, AGWs tend towards acoustic wave mode, and when the frequency is  
63 much smaller than the buoyancy frequency, the fluid can be considered incompressible, and  
64 the AGWs tend towards internal GWs mode. The term “acoustic-gravity waves” is usually  
65 used when restoring forces due to both gravity and compressibility are important. AGWs  
66 are known to play a significant role in the coupling between the atmosphere/ionosphere and  
67 the ocean (Press and Harkrider, 1962; Harkrider and Press, 1967; Donn and Balachandran,  
68 1981; Azeem et al., 2017). Atmospheric pressure waves are mechanical waves that are  
69 related to the density of the atmosphere. Compression and expansion are the high-pressure  
70 and low-pressure regions of motion in a medium.

71 The 2022 HTHH volcano eruption triggered tsunamis that affected the whole world  
72 (Carvajal et al., 2022; Ghent et al., 2022). Conventional tsunamis are typically generated by  
73 localized sea surface displacements caused by sources such as earthquakes and volcanoes,  
74 similar to the tsunamis directly induced by the 2022 Tonga volcano eruption (TITVE).  
75 Another tsunami is induced by the atmospheric pressure wave (TIAPW) (Kubota et al.,  
76 2022; Gusman et al., 2022). Tsunami can generate upward propagating AGWs through  
77 water-air interface and propagate to the thermosphere/ionosphere (Hines, 1972; Peltier and  
78 Hines, 1976; Hickey et al., 2009, 2010; Occhipinti et al., 2013; Vadas et al., 2015;  
79 Laughman et al., 2016; Nishikawa et al., 2023; Pradipta et al., 2023). Using the red line

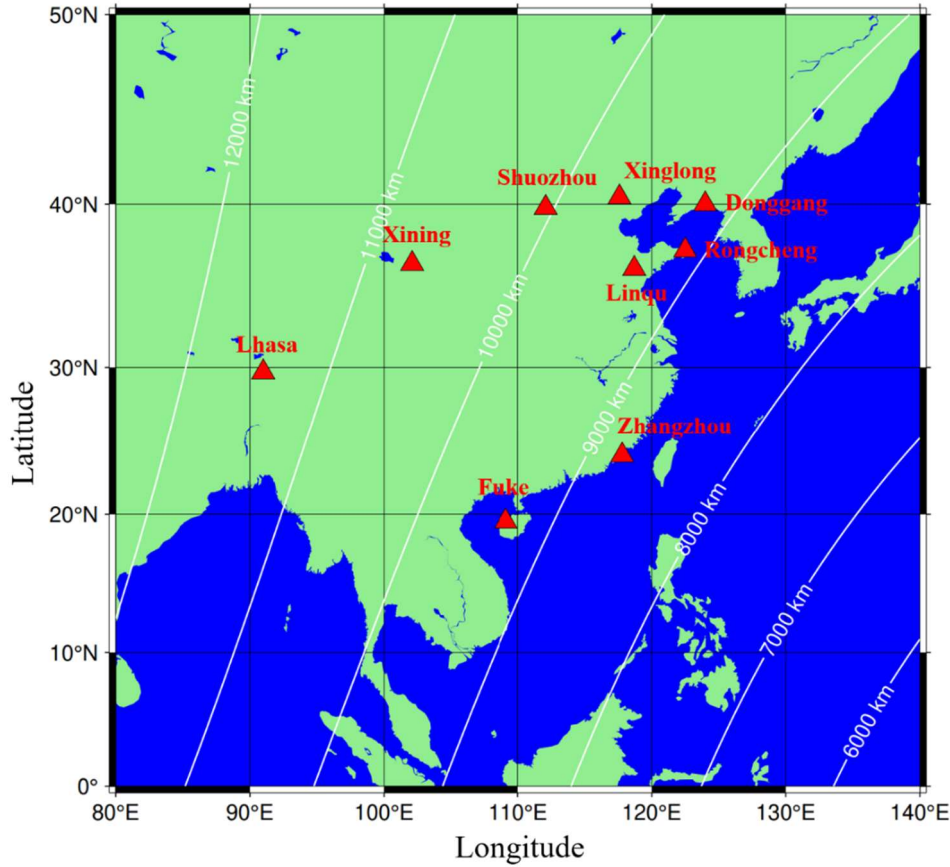
80 airglow imager, Makela et al. (2011) detected airglow disturbance in Hawaii that arrived  
81 1hr earlier of the tsunami generated by the 11 March 2011 Tohoku earthquake. Also using  
82 the redline airglow, Smith et al. (2015) observed tsunami and GW almost simultaneously in  
83 Chile. Inchin et al. (2020) used a three dimensional (3D) numerical model to simulate the  
84 atmospheric AGWs generated by tsunami. They found that bathymetry variations  
85 significantly affected the tsunamis and the AGWs excited by tsunamis, leading to their  
86 nonlinear evolution process. More recently, Inchin et al. (2022) performed the numerical  
87 simulations of mesopause airglow radiation fluctuations induced by tsunami-generated  
88 AGWs, and found that large-scale tsunamis can cause detectable and quantitative  
89 disturbances of mesopause airglow through AGWs.

90 As far as we know, the research on the impact of tsunamis induced atmospheric  
91 AGWs on the atmosphere and ionosphere shown above is all caused by conventional  
92 tsunami. There are only two rare studies on the ground-based airglow observations of  
93 AGWs caused by this conventional tsunami, and both are limited to red line observations  
94 (Makela et al., 2011; Smith et al., 2015). However, the observation of tsunami induced  
95 AGWs in the mesopause region observed by ground-based airglow imaging has never been  
96 reported. In this study, we first reported the propagation characteristics of the AGWs  
97 generated by the tsunamis triggered by the 2022 HTHH volcano eruptions in the  
98 mesopause region using the ground-based airglow imager observation network. We then  
99 focus on the coupling process of atmospheric pressure waves triggering tsunamis, and then  
100 tsunamis generating atmospheric AGWs through air-water-air-coupling process in the  
101 far-field area of the 2022 HTHH volcano eruption.

## 102 **2. Data and Methods**

### 103 **2.1 Multi layer airglow imager network**

104 A multi-layer airglow observation network (Xu et al., 2021) was built to study  
105 atmospheric disturbances excited by severe weather events, such as thunderstorms (Xu et  
106 al., 2015), typhoons (Li et al., 2022) and volcanic activities. Figure 1 shows the distribution  
107 of the multi-layer airglow observation network station. The multi-layer airglow observation  
108 network mainly includes the OH airglow network, which has been used to observe the  
109 airglow layer at the height of 87 km; the OI airglow network has been used to observe the  
110 airglow layer at the height of 250 km. In addition, there were 557 nm airglow and Na  
111 airglow imagers installed at some stations, such as Xinglong Station (40.4°N, 117.6°E),  
112 Lhasa (29.7°N, 91.0°E). The airglow network can provide observation with high temporal  
113 and spatial resolution. The temporal resolution is 1 min and the spatial resolution is 1 km.  
114 The time resolution of OH airglow imager is 1 minute, while the resolution of OI 557 nm  
115 and OI 630 nm airglow imager is 3 minutes, respectively. The spatial resolution of the  
116 airglow imager at the airglow layer is not uniform. The resolutions of OH, OI 557 nm, and  
117 OI 630 nm airglow in the zenith direction are 0.27 km, 0.29 km, and 0.77 km, respectively,  
118 while in the zenith angle of 60°, the resolutions are 1.01 km (OH), 1.11 km (OI 557 nm),  
119 and 2.65 km (OI 630 nm), respectively.

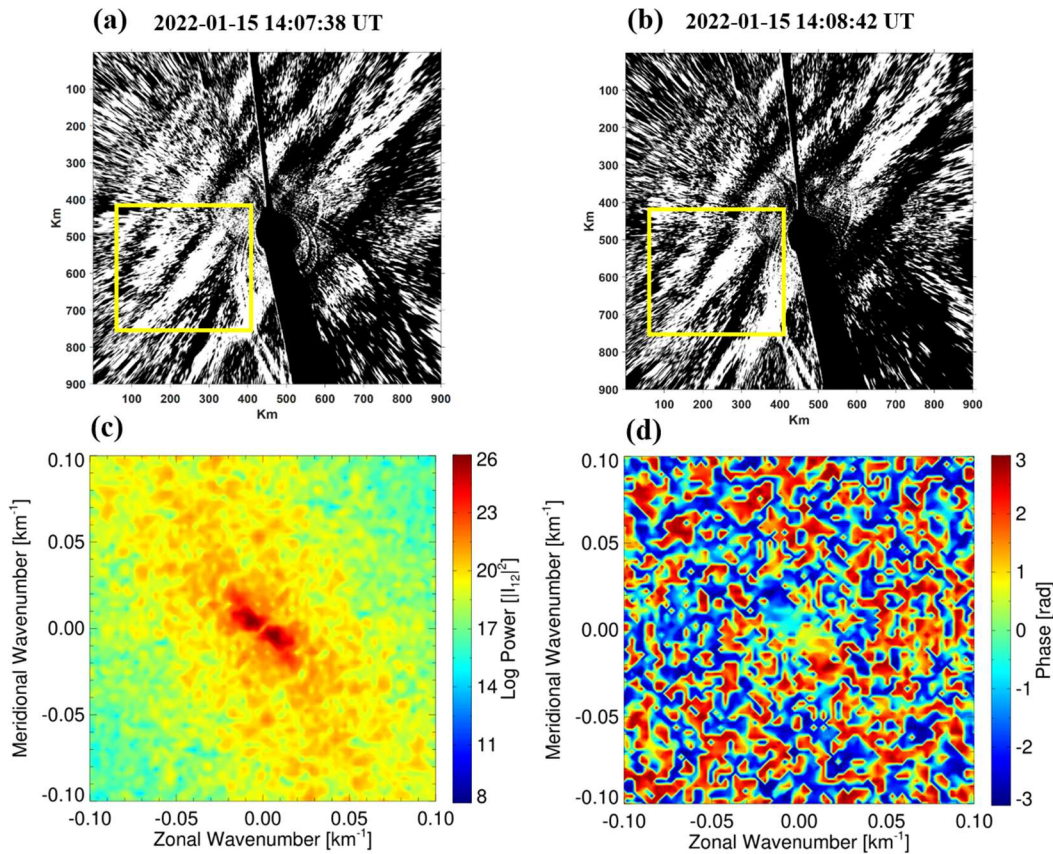


120  
 121 **Figure 1** The distribution of airglow network stations, along with the large circular centered on the  
 122 Tonga volcano and its radius length, is also marked in the figure.

123 **2.2 Spectral analysis of atmospheric wave parameters**

124 The airglow image was calibrated with the help of standard star map (Garcia et al.,  
 125 1997) and projected into geospatial space. The background radiation is removed by time  
 126 differential (TD) method (Swenson and Mende, 1994), to highlight atmospheric  
 127 fluctuations. The atmospheric wave parameters (horizontal wavelength  $\lambda_h$ , observed  
 128 horizontal phase speed  $c$ , and the relative intensity perturbation  $I'/I$ ) are extracted from  
 129 spectral analysis method. Figure 2c presents the two-dimensional cross spectrum obtained  
 130 from Fig. 2a and 2b. Zonal ( $k_x$ ) and meridional ( $k_y$ ) wave numbers are determined from  
 131 the peak position of the spectra. The horizontal wavelengths  $\lambda_h$  are obtained from the  
 132 expression of  $\lambda_h = 2\pi / \sqrt{k_x^2 + k_y^2}$ . The observed speeds  $c$  are calculated from the phase ( $\varphi$ )

133 (Fig. 2d) at the maximum peak of the cross spectrum as  $c = \frac{\varphi}{2\pi} \frac{\lambda_h}{\Delta t}$ , where  $\Delta t$  is the time  
 134 interval between the two TD images. The amplitudes of intensity perturbations were  
 135 calculated by integrating the power surrounding the central peaks of the power spectrum.  
 136 To eliminate noise, the energy of the wave spectrum should be greater than 10% of the total  
 137 spectrum (Tang et al., 2005).



138  
 139 **Figure 2** The time difference images (a-b) obtained from the Xinglong OH airglow imager on the night  
 140 of 15 February 2022. Each image is projected on an area of 900 km × 900 km. The (c) cross spectrum  
 141 and (d) phase obtained from the yellow box area in the (a) and (b) using 2-D fast Fourier transform.

### 142 2.3 Tsunami simulation model

143 Tonga submarine volcano erupted on 15 January 2022, and generated tsunamis that  
 144 were detected around the globe, affected particularly the Pacific region. In this study, two  
 145 types of tsunamis were simulated, conventional tsunami simulations and atmospheric  
 146 pressure wave-induced tsunami simulations. The linear-shallow water equations in the



147 spherical coordinate system are used to simulate the tsunamis from the localized source and  
 148 atmospheric pressure wave. The continuity equation of a linear shallow water wave model  
 149 in spherical coordinates is:

$$150 \quad \frac{\partial \eta}{\partial t} + \frac{1}{R \sin \theta} \left[ \frac{\partial(ud)}{\partial \varphi} + \sin \theta \frac{\partial(vd)}{\partial \theta} \right] = 0 \quad (1)$$

151 where  $\eta$  is free surface elevation (m),  $d$  is the water depth (m),  $R$  is the Earth's  
 152 radius (6371,000 m),  $\varphi$  is longitude,  $\theta$  is colatitude.

153 While the momentum equations of the linear shallow water wave model are:

$$154 \quad \frac{\partial u}{\partial t} + \frac{1}{R \sin \theta} \left[ g \frac{\partial \eta}{\partial \varphi} + \frac{1}{\rho} \frac{\partial p}{\partial \varphi} \right] + fv = 0 \quad (2)$$

$$155 \quad \frac{\partial v}{\partial t} + \frac{1}{R} \left[ g \frac{\partial \eta}{\partial \theta} + \frac{1}{\rho} \frac{\partial p}{\partial \theta} \right] - fu = 0 \quad (3)$$

156 where,  $u$  is the velocity along the lines of longitude (m/s),  $v$  is the velocity along  
 157 the lines of latitude,  $g$  is the gravitational acceleration (9.81 m/s<sup>2</sup>),  $p$  is the  
 158 atmospheric pressure (Pa),  $\rho$  is the sea water density (1026 kg/m<sup>3</sup>),  $f$  is the Coriolis  
 159 coefficient. For the atmospheric pressure wave-induced tsunami simulation, the moving  
 160 change pressure terms as an input to tsunami simulation momentum equation. The  
 161 atmospheric pressure wave model is based on the Equation (1) in Gusman et al. (2022).

162 For the tsunami simulations from a localized source, a B-spline function (Koketsu and  
 163 Higashi, 1992) below is used to represent the circular water uplift source at the volcano:

$$164 \quad f(x, y) = \sum_{i=0}^3 \sum_{j=0}^3 c_{k+i, l+j} B_{4-i} \left( \frac{x-x_k}{h} \right) B_{4-j} \left( \frac{y-y_l}{h} \right) \quad (4)$$

165 where  $B_i(r) = \begin{cases} r^3/6, & i=1 \\ (-3r^3 + 3r^2 + 3r + 1)/6, & i=2 \\ (3r^3 - 6r^2 + 4)/6, & i=3 \\ (-r^3 + 3r^2 - 3r + 1)/6, & i=4 \end{cases}$  (5)

166  $x_k$  and  $x_l$  stand for the coordinates of the knots along the x and y axes, h is the  
 167 characteristic diameter of water uplift,  $r$  is the great-circle distance from the volcano  
 168 eruption center,  $c_{1,1} = 1$  and the other  $c_{k+i,l+j} = 0$ . In this study, the modelling domain covers  
 169 the Pacific Ocean and some parts of Indian Ocean and the Caribbean with a grid size of 5  
 170 arc-min. For detailed tsunami simulation algorithms, please refer to Gusman et al. (2022).  
 171 The models for the 2022 HTHH volcanic eruption used in this study was estimated and  
 172 validated with observations at offshore DART stations around the Pacific Ocean in a  
 173 previous study (Fig. 3 and Fig. 7 of Gusman et al., 2022).

#### 174 2.4 Ray tracing method

175 The following ray tracing equations (Lighthill, 1978) describes the propagation path of  
 176 AGWs.

177 
$$\frac{dx_i}{dt} = \frac{\partial \omega}{\partial k_i} = c_{g_i}$$
 (6)

178 
$$\frac{dk_i}{dt} = -\frac{\partial \omega}{\partial x_i}$$
 (7)

179 where  $x_i$ ,  $k_i$ ,  $c_{g_i}$  ( $i=1, 2, 3$ ), and  $\omega$  are the position vector, wavenumber vector,  
 180 group speed, and intrinsic frequency, respectively.

181 Using the dispersion relation of acoustic gravity wave (Yeh and Liu, 1974), we can  
 182 assess the vertical propagation state of AGWs. The dispersion relation is as follows

183 
$$m^2 = \frac{\omega^2}{c_s^2} \left(1 - \frac{\omega_a^2}{\omega^2}\right) - k^2 \left(1 - \frac{\omega_b^2}{\omega^2}\right)$$
 (8)

184 where  $m$  is the vertical wave number,  $k$  is the horizontal wave number,  $c_s$  the local speed of  
185 sound,  $\omega = k(c - u)$  is intrinsic frequency,  $u$  is the background wind speed in the direction of  
186 wave propagation from meteor radar observations and ERA-5 (Hersbach et al., 2020).

187  $\omega_a^2 = \frac{g}{T} \frac{dT}{dz} + \frac{\gamma g}{4H}$  is acoustic cutoff frequency,  $\omega_b^2 = \frac{g}{T} \frac{dT}{dz} + \frac{(\gamma - 1)g}{\gamma H}$  is buoyancy frequency,

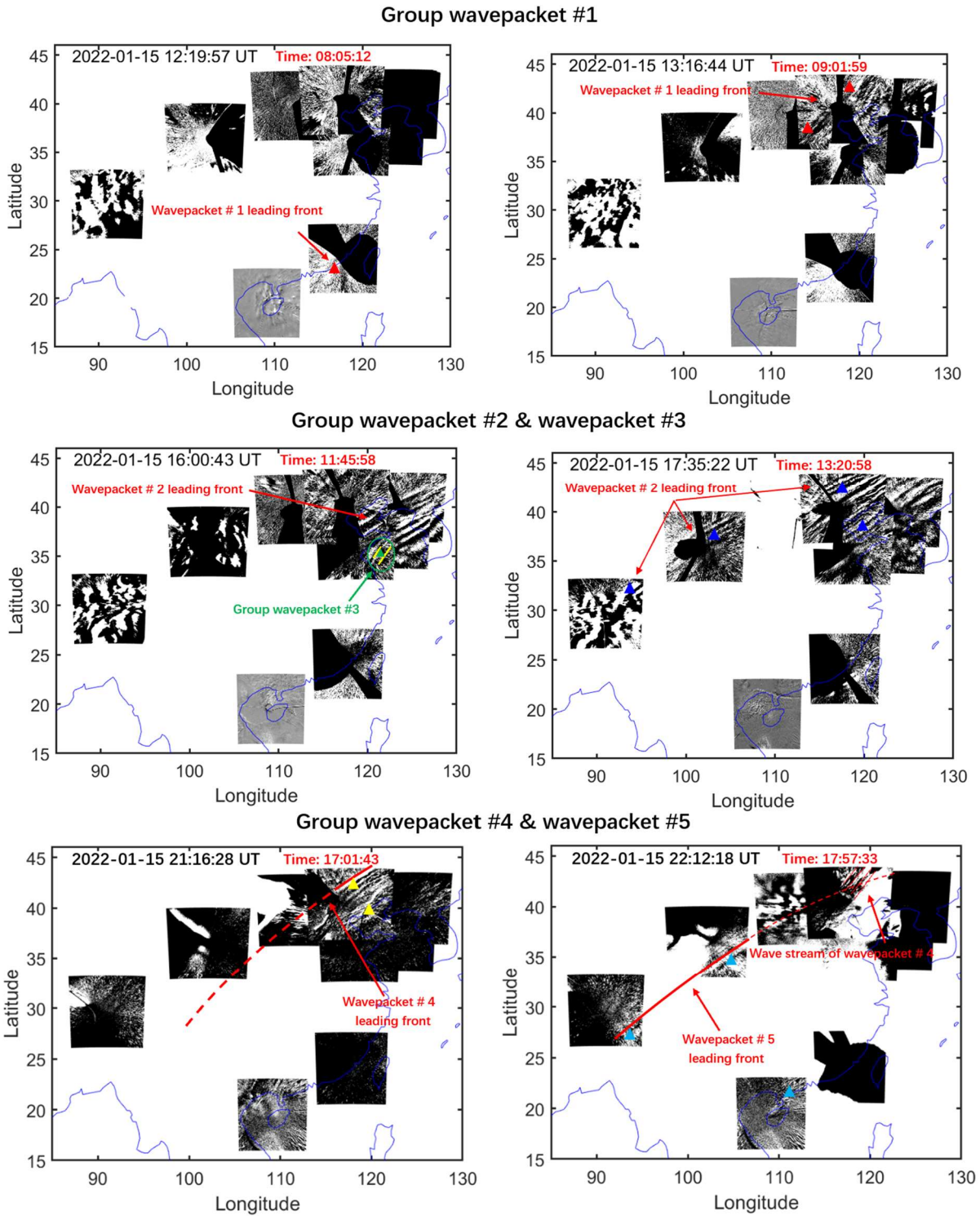
188  $g$  is the gravitational acceleration, and  $T$  is temperature from the Sounding of the  
189 Atmosphere using Broad band Emission Radiometry (SABER) instrument on the  
190 Thermosphere Ionosphere Mesosphere Energetics and Dynamics (TIMED) satellite. When  
191  $\omega > \omega_a$  or  $\omega < \omega_b$ ,  $m^2 > 0$ , AGW can propagate freely, while when  $\omega_b < \omega < \omega_a$ ,  $m^2 < 0$ , the wave is  
192 evanescent.

### 193 **3. Results and Discussion**

#### 194 **3.1 Upper Atmospheric Airglow Responses to HTHH Volcanic Eruption via Lamb** 195 **Waves**

196 Five groups of atmospheric waves (wave packets #1-5) were observed in the  
197 mesopause region by the ground-based airglow network. Refer to this Supplement  
198 (<https://doi.org/10.5446/66190>) for detailed wave propagation status. To eliminate random  
199 disturbances, we also made videos of two days before and after the volcanic eruption  
200 (<https://av.tib.eu/series/1689>). From the videos, it can be seen that the OH airglow layer  
201 was very calm during this period. Figure 3 shows the wave packet #1 observed by the  
202 airglow imager network (top panels). Wave packet #1 entered the view of the airglow  
203 network approximately 8 hr after the HTHH volcanic eruption (Left image of top panels).  
204 Three hours after wave packet #1 entered the field of view, wave packet #2 was observed  
205 by the airglow network. The leading front of wave packet #2 has an uninterrupted

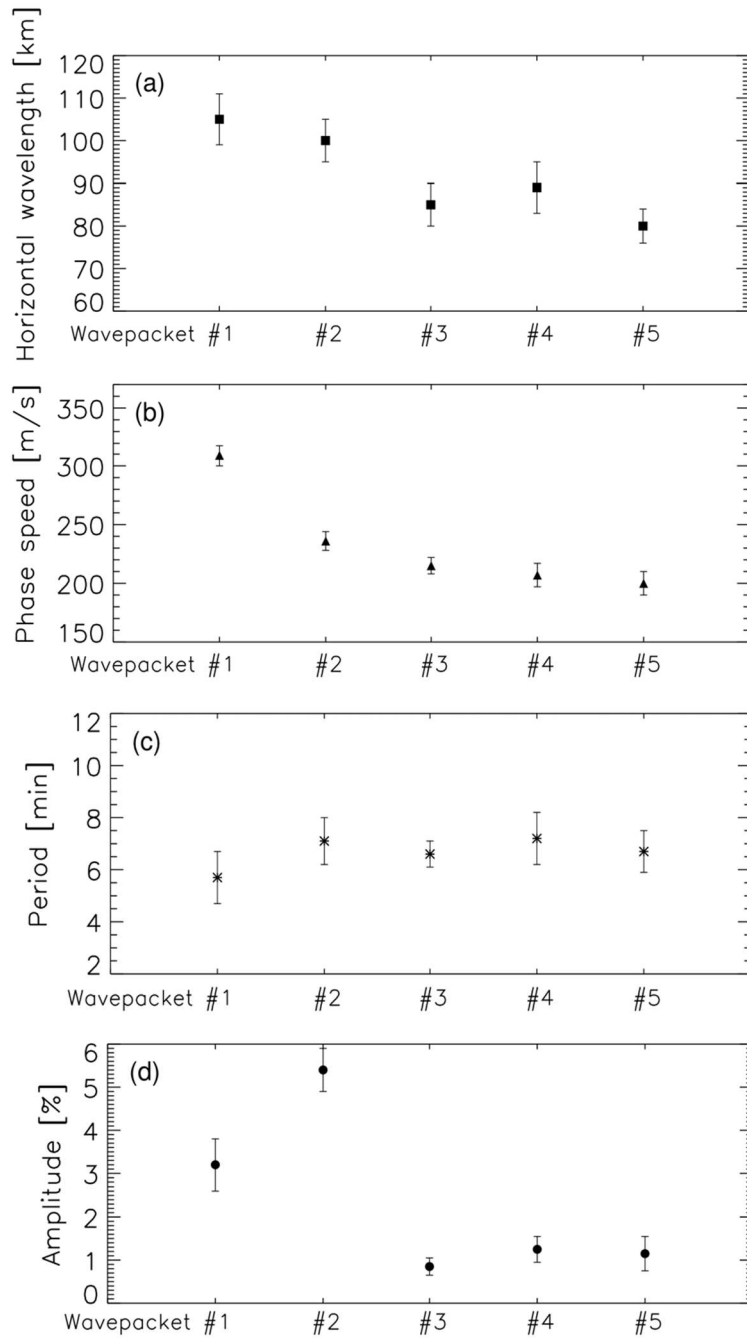
206 continuous front, which almost covers the whole Chinese Mainland (middle panels).  
207 Interestingly, we observed AGWs accompanying wave packet #2 (hereafter wave packet #3)  
208 over the northwest region of the Yellow Sea (Left image of middle panels). Wave packet #2  
209 always keeps a stable state in the process of propagation, and maintains a regular front  
210 when propagating over Lhasa Station (29.7°N, 91.0°E). Wave packet #4 exhibits strong  
211 instability characteristics during propagation. Compared to the continuous leading front of  
212 wave packet #2, the fronts of wave packets #4 and #5 are separated (bottom panels). We  
213 also found that wave packet #5 propagate more than 3000 km inland (propagating to the  
214 area west of longitude 90°E).



215  
 216 **Figure 3** Five strong group atmospheric waves associated with the Tonga volcano eruptions were  
 217 observed in the mesopause region by the ground-based airglow network. Different colored triangles  
 218 correspond to each wave event sampling point, while red, blue, green, yellow, and cyan correspond to  
 219 wavepackets #1, #2, #3, #4, and #5, respectively. The red time markers in this figure and the following  
 220 figure represent the lapse time since the volcano eruption.

221 Figure 4 shows the distribution of wave parameters for multi-group of atmospheric

222 waves (wave packets #1-#5) from cross spectral analysis. The phase speed of wave packet  
223 #1 leading front is approximately 309 m/s. Wave packet #2 displays a slightly slower phase  
224 speed, with average phase speed of 236 m/s. The horizontal phase speeds of group wave  
225 packets # 3-5 are mainly distributed in the range of 200 m/s to 215 m/s, which is smaller  
226 than that of wave packets # 1-2. The horizontal wavelengths of these five group wave  
227 packets are mainly distributed in 80 km-105 km, while the observation periods are  
228 relatively small and mainly concentrated in 5.7 min-7.2 min. For amplitude, the average  
229 amplitude of the lamb wave L1 mode (5.4%) is higher than that of the lamb wave L0 mode  
230 (3.2%). Wavepackets # 3, # 4, and # 5 have relatively small amplitudes, mainly distributed  
231 between 0.85% and 1.25%.



232  
 233 **Figure 4** Distribution of (a) horizontal wave wavelength, (b) phase speed, (c) period, and (d) amplitude  
 234 parameters for multi-group of atmospheric waves (wave packets #1-#5). The calculation of wave packet  
 235 parameters comes from the average value of the wave passing through the sampling points in Fig 3.

236 The HTHH volcano eruption produced Lamb waves that propagate around the globe,  
 237 (Wright et al., 2022) causing sudden changes in surface pressure (Omira et al, 2022;  
 238 Takahashi et al., 2023). Figure 5f shows the surface air pressure data of Xinglong station  
 239 (40.4°N, 117.6 °E). At 13:15 UT on January 15, 2022, the air pressure dropped sharply from

240 920 Pa to 917.7 Pa, indicating that Lamb wave arrived at the surface of Xinglong station at  
241 13:15 UT. A small disturbance of air pressure occurs at 16:33 UT. Figures 5e and 5d present  
242 Himawari-8 6.2  $\mu\text{m}$  brightness temperature at 13:10:00 UT (Otsuka, 2022). It can be seen  
243 that the leading front of Lamb wave L0 mode happens to pass through the zenith direction  
244 of Xinglong station. The time when wave packet #1 (Fig. 5b) and wave packet #2 (Fig. 5c)  
245 reach the zenith direction of Xinglong Station from OH airglow observation is 13:13:34 UT  
246 and 16:32:16 UT, which matches the time for surface pressure disturbances quite well. The  
247 phase speed of the wave packet #1 leading front ( $\sim 309$  m/s) is very close to the speed of  
248 surface Lamb wave (L0 mode). From the Fig 5, it can be seen that the phase of the lamb  
249 wave L0 mode is almost vertical from the ground to the stratosphere and then to the  
250 mesosphere. The wave packet # 2 with a slower phase speed ( $\sim 236$  m/s) is consistent with  
251 the Lamb wave L1 mode in theoretical predictions (Francis, 1973) and simulations from  
252 WACCM-X model (Liu et al., 2023). However, at almost the same time, the wave front  
253 observed in the thermosphere (Video Supplement, <https://doi.org/10.5446/66280>) with a  
254 slightly faster phase speed of 342 m/s is nearly 550 km a head of the wave front in the  
255 mesopause region in the horizontal propagation direction and ahead of time approximately  
256 30 min (Fig. 5a). This is in good agreement with theoretical and modeling results (Fig. 4 of  
257 Lindzen and Blake, 1972; Fig. 2 of Liu et al. 2023), which show that the wave fronts of  
258 Lamb wave below the lower thermosphere are vertical and tilt forward above. As for Lamb  
259 wave L1 mode, the ground and mesopause region provide waveguide surfaces, resulting in  
260 maximum wave energy between the two layer, while the phase does not change with height  
261 (Francis, 1973).

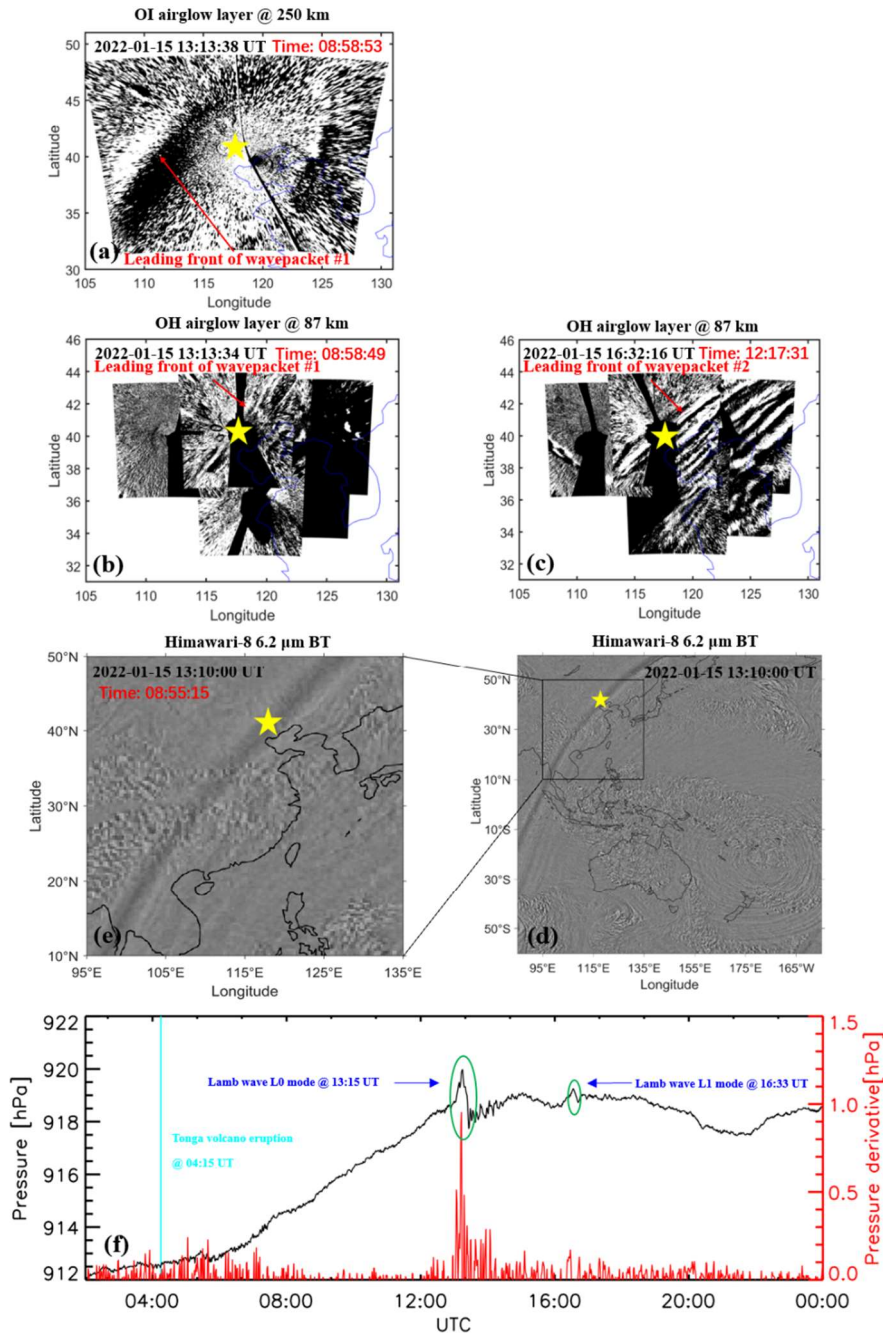


262 As for why the observed Lamb wave L0 shape in the OH airglow layer is not a strong  
263 leading wave with much weaker trailing waves, it may be caused by the following factors.  
264 It is seen from model simulations that the wave amplitudes of L0 and L1 modes are not  
265 uniform at the wave front. This non-uniformity becomes more pronounced in the upper  
266 atmosphere (e.g. Fig 2 of Liu et al., 2023), probably as a result of the large variation of the  
267 background atmosphere propagation conditions. It is thus possible that over certain regions  
268 the trailing waves become comparable with the leading wave. It is also possible for the  
269 leading wave to gradually dissipate energy and become invisible during propagation by  
270 generating trailing waves. In addition, due to the smaller field of view of the airglow  
271 imager compared to satellite observations, some structures may be related to local fine  
272 structures, especially in the middle and upper layers where many internal waves have  
273 significant amplitudes, which may be relatively more significant than Lamb waves.

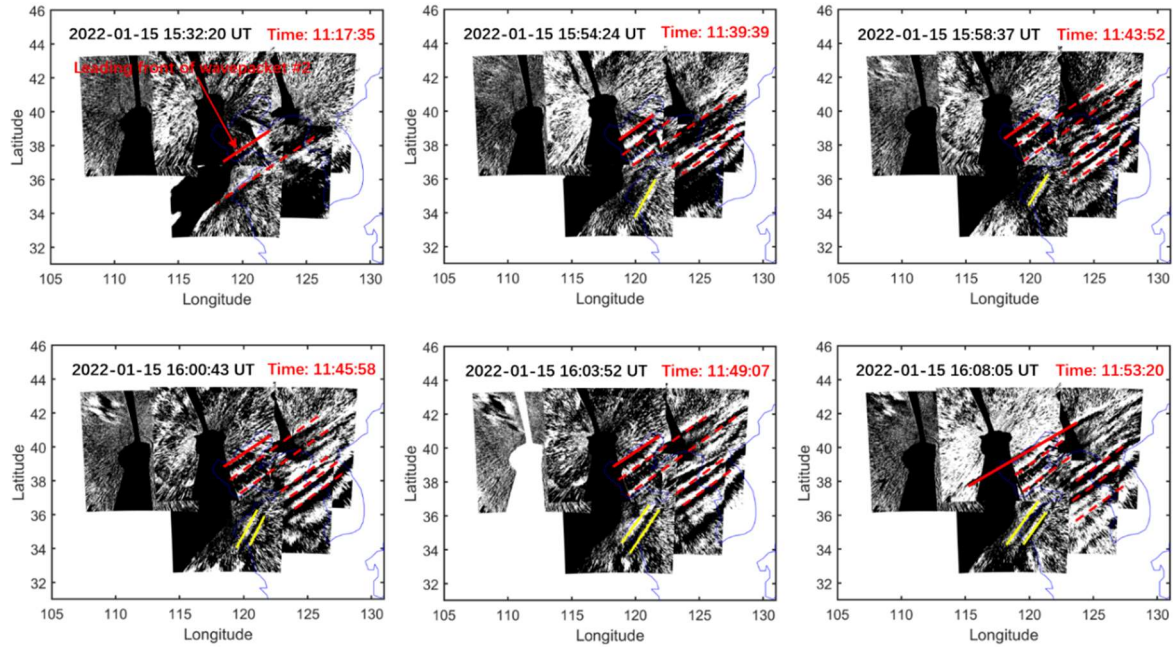
274 As mentioned above, the amplitude of Lamb wave L1 mode in the mesopause region  
275 is greater than that of L0 mode, which may be due to the fact that L1 mode is an internal  
276 wave below the mesopause (Liu et al. 2023). For an isothermal atmosphere, the Lamb wave  
277 L0 mode amplitude grows with altitude  $z$  as  $e^{\kappa z/H}$ , where  $H$  is the scale height,  $\kappa = (\gamma - 1)/\gamma$ ,  
278 and  $\gamma$  is the ratio of specific heats ( $\sim 1.4$ ). However, the amplitude of internal GWs varies as  
279  $e^{z/2H}$ . The amplitude of internal waves increases with height at a rate greater than that of  
280 surface modes.

281 Poblet et al. (2023) reported observation of Lamb wave L1 mode in the horizontal  
282 wind field of meteor radar, but they do not see Lamb wave L0 mode and argue that L0 mode  
283 is likely a higher-frequency wave and got averaged out. Stober et al. (2018, 2024) found

284 that the anomalous peak signal in the meteor radar wind field cannot be completely  
285 determined to be caused by the Lamb wave generated by the Tonga volcanic eruption. On  
286 the one hand, meteor radar observations may have filtered out high-frequency Lamb waves.  
287 On the other hand, even if Lamb waves are observed in the upper atmosphere, there is still  
288 debate over whether they propagate directly to the upper atmosphere or through multi-step  
289 vertical coupling process described by Becker and Vadas (2018), Vadas and Becker (2018),  
290 and Vadas et al. (2018, 2023).



291  
 292 **Figure 5** (a) OI 630 nm airglow observation at 13:13:18 UT. OH airglow network observations when (b)  
 293 wave packet #1 and (c) wave packet #2 pass through the zenith direction of Xinglong Station at 13:13:34  
 294 UT and at 16:32:16 UT, respectively. (d)-(e) Himawari-8 6.2  $\mu\text{m}$  brightness temperature at 13:10:00 UT.  
 295 (f) The surface time series of surface pressure obtained from Xinglong observation station. The red line  
 296 represents the time derivative of the pressure. The sudden change of air pressure at 13:15 UT indicates  
 297 the arrival time of Lamb wave L0. A small disturbance of air pressure occurs at 16:33 UT indicates the  
 298 arrival time of Lamb wave L1. The yellow stars represent the location of the Xinglong station.



299  
 300 **Figure 6** The red solid lines indicate leading wave front of the wave packet #2. The yellow solid lines  
 301 mark wave packet #3, which are clearly not parallel to the wave fronts of wave packet #2.

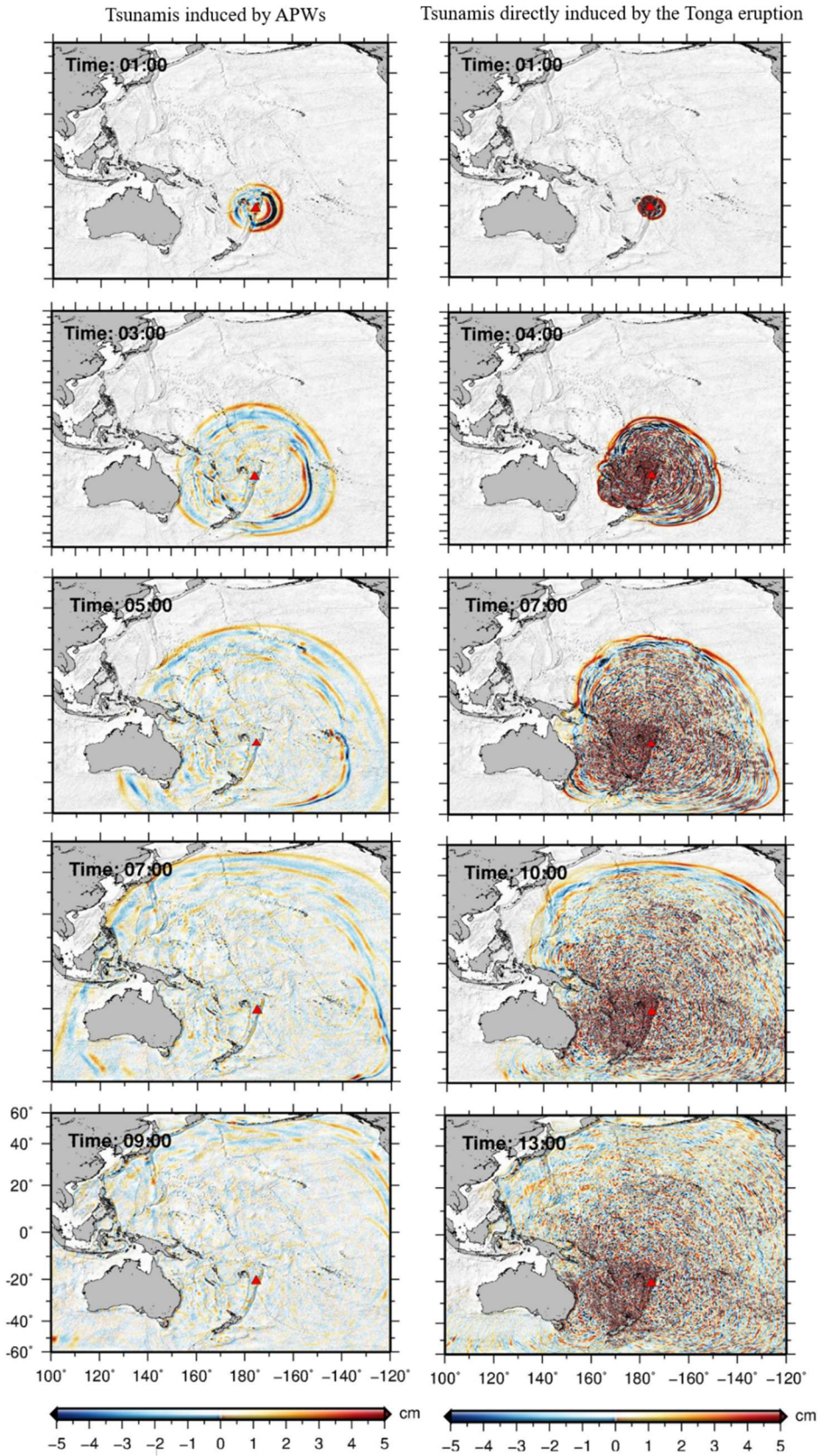
302 Figure 6 shows the time sequence of propagation image of wave packet #3. We found  
 303 that with the propagation of wave packet #2, there is an AGW (wave packet #3) with a  
 304 certain angle between its phase plane (yellow solid line) and the phase plane of wave  
 305 packet #2. This implies that the source of the wave packet #3 is different from that of wave  
 306 packet #2. The horizontal wavelength of the wave packet #3 near the coast is  $84 \text{ km} \pm 5$   
 307 km.

### 308 **3.2 Simulation of Tsunami induced by HTHH Volcano Eruption**

309 The 2022 HTHH volcano eruption triggered global atmospheric pressure waves. The  
 310 simulated atmospheric pressure waves propagate at an approximate constant speed of 317  
 311 m/s, and the amplitude decreases with the distance from the volcano (Gusman et al., 2022).  
 312 Figure 7 shows snapshots of the TIAPW and TITVE simulation results. The leading  
 313 TIAPW excited by the pressure disturbances travels at the same speed as the atmospheric

314 pressure wave and is followed by subsequent sea waves generated earlier in the  
315 atmospheric pressure wave propagation which thereafter travel at the conventional tsunami  
316 propagation speed. Under a given pressure gradient, the discharge flux in deep sea is much  
317 greater than that in shallow water. A deep bathymetric feature such as the Kermadec Tonga  
318 Trench can more effectively generate tsunami waves. The wave train following the leading  
319 wave travelling over the trench appear to be larger than those travelling in other directions.  
320 The propagation speed of TITVE from the shallow water (long) wave approximation is  
321  $v = \sqrt{gH_0}$  (Salmon, 2014), where  $g$  is the gravitational acceleration and  $H_0$  is the ocean  
322 depth. For sea water with a general depth of 4 km, the speed of shallow water wave is about  
323 200 m/s. Therefore, the TIAPW is significantly faster than the TITVE. The amplitude of  
324 TITVE is greater than that of tsunamis generated by atmospheric pressure waves. The wave  
325 train following the leading wave of TITVE exhibit finer structures with scales smaller than  
326 that of TIAPW. We found that the TIAPW arrived along the coast of Chinese Mainland  
327 about 4-5 hours earlier than the TITVE.



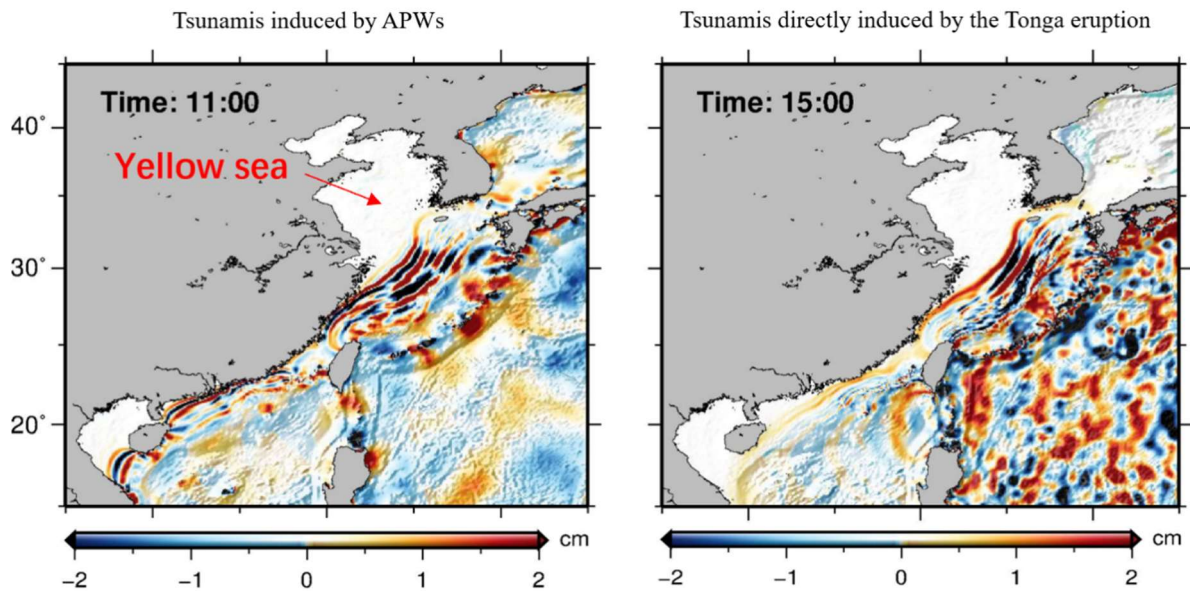


328  
 329 **Figure 7** Snapshots of simulated tsunamis induced by the atmospheric pressure wave (left panels) and  
 330 tsunamis directly induced by the Tonga volcano eruption (right panels).

### 331 3.3 Upper atmosphere responses to HTHH volcanic eruption via Air-Sea Interaction

332 Figure 8 shows the simulation results of TIAPW and TITVE near the coast of Chinese  
333 Mainland 11 hr (15:15 UT) and 15 hr (19:15 UT) after the volcanic eruption, respectively.  
334 Air pressure waves are not very efficient at directly exciting tsunamis in shallow water due  
335 to the weaker air-sea coupling (Gusman et al., 2022; Yamada et al., 2022). The Yellow sea  
336 is quite shallow, so the amplitude of the leading of TIAPW is very small there. The leading  
337 wave is followed by subsequent waves with larger amplitudes, which propagate in the same  
338 direction as the leading wave but at the conventional tsunami speed (Gusman et al., 2022).  
339 We found that the TIAPW and TITVE on the continental shelf have shorter wavelengths  
340 compared with those in the deep ocean. When the tsunamis approached the coast of China,  
341 three groups of AGWs (wave packet #3 and wave packets #4-5) were observed by the  
342 airglow network. The time when the AGW entered the view of the airglow network was  
343 very close to the time when the Tonga tsunamis reached the coast of Chinese Mainland.  
344 The wave packet #3 entered the airglow network at 15:30 UT and the wave packets #4-5  
345 entered the airglow network at 19:40 UT. This strongly suggests that the wave packets  
346 detected by the airglow network are correlated to the tsunamis near the coast. We found that  
347 as the tsunamis approached the coast of China, they diffracted between Taiwan and  
348 Philippines and became discontinuous. And the wave packets #4 and #5 we observed was  
349 also discontinuous, which further confirms the correlation between wave packets # 4-5 and  
350 discontinuous tsunamis. We estimate that the average wavelength of TIAPW near the coast  
351 of the Yellow Sea is approximately  $82 \text{ km} \pm 4 \text{ km}$ , which is very consistent with the  
352 horizontal wavelengths of the atmospheric AGW observed by airglow network as mention

353 above ( $84 \text{ km} \pm 5 \text{ km}$ ), while the average wavelengths of TITVE near the coast of the  
 354 Yellow Sea and South Sea are  $95 \pm 5 \text{ km}$  and  $86 \pm 5 \text{ km}$ , respectively.

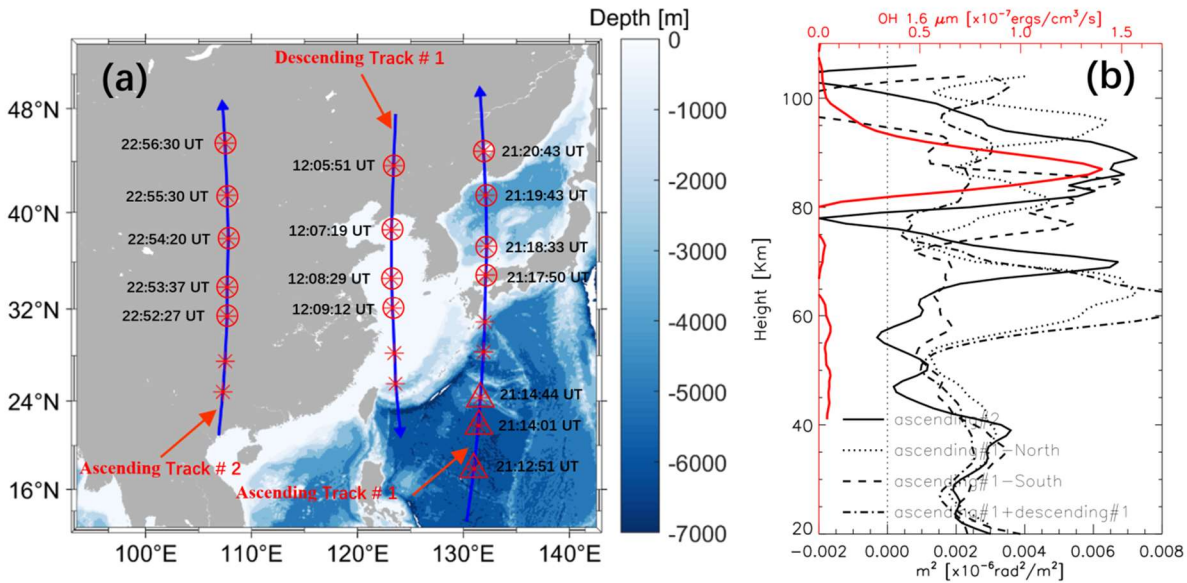


355  
 356 **Figure 8** Simulated tsunamis induced by the atmospheric pressure wave (left panels) and tsunamis  
 357 directly induced by the Tonga volcano eruption (right panels) near the coast of Chinese Mainland. The  
 358 marked time represents the time after the volcanic eruption.

359 Figure 9a shows three TIMED satellite tracks with descending track #1 along the coast  
 360 of China, ascending track #1 located east of the Korean Peninsula, and ascending track #2  
 361 inland China. Figure 9b shows the square of vertical wave number  $m^2$  profile (black)  
 362 derived from the average temperature from the limb viewing of the Sounding of the  
 363 Atmosphere using SABER/ TIMED measurement locations marked by the red circles and  
 364 triangles in Fig. 9a. We take the average temperature of ascending track #1 and descending  
 365 track #1 serves as the background temperature for the wave packet #3 and ascending track  
 366 #1 as the background temperature of the wave packets #4-5 when they propagate in the  
 367 coastal vicinity. We take ascending track #2 as the background temperature of wave packets  
 368 #4-5 when they propagate inland China. The peak height of OH airglow layer is 87 km. We  
 369 found that the propagation of wave packet #3 (dash-dotted line) is in a state of free



370 propagation in the coastal vicinity.

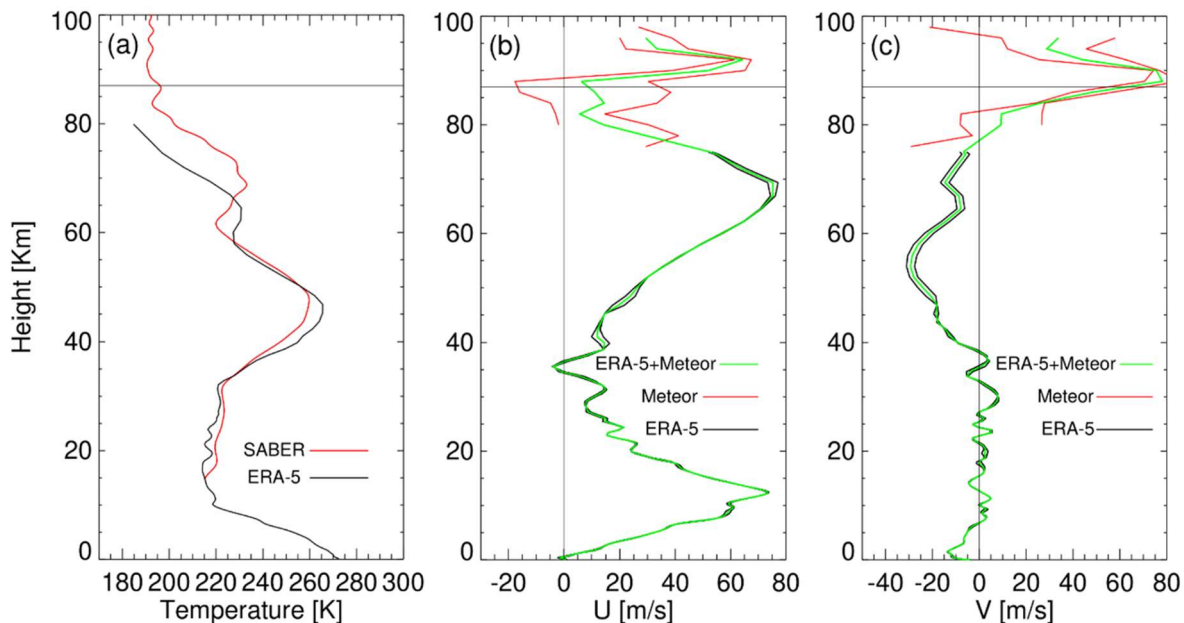


371  
 372 **Figure 9** (a) Ascending and descending SABER/TIMED satellite tracks over Chinese Mainland.  
 373 Background representative ocean depth map. (b) Square of vertical wave number  $m^2$  profiles: black solid  
 374 line profile derived from the ascending track #2 (marked by the red circle), dotted line profile derived  
 375 from the ascending track #1-North (marked by the red circle), dashed line profile derived from the  
 376 ascending track #1-South (marked by the red triangle), and dash-dotted line profile derived from the  
 377 average the ascending track #1 and descending track #1 (marked by the red circle) from the  
 378 SABER/TIMED measurement locations in (a). The red line represents the OH 1.6  $\mu\text{m}$  emission intensity  
 379 obtained by the SABER/TIMED.

380 Figure 10 show the background field used for ray tracing analysis for the TIAPW  
 381 event. The temperature comes from TIMED/SABER and ERA-5 and wind data from  
 382 meteor radar and ERA-5. Meteor radar wind field is from Beijing station (40.3°N, 116.2°E).  
 383 Figure 11 shows the results of ray tracing for the wave packet #3. We find that the source  
 384 location of AGWs over the coast of Chinese Mainland falls in the near coast where the  
 385 tsunami occurred.

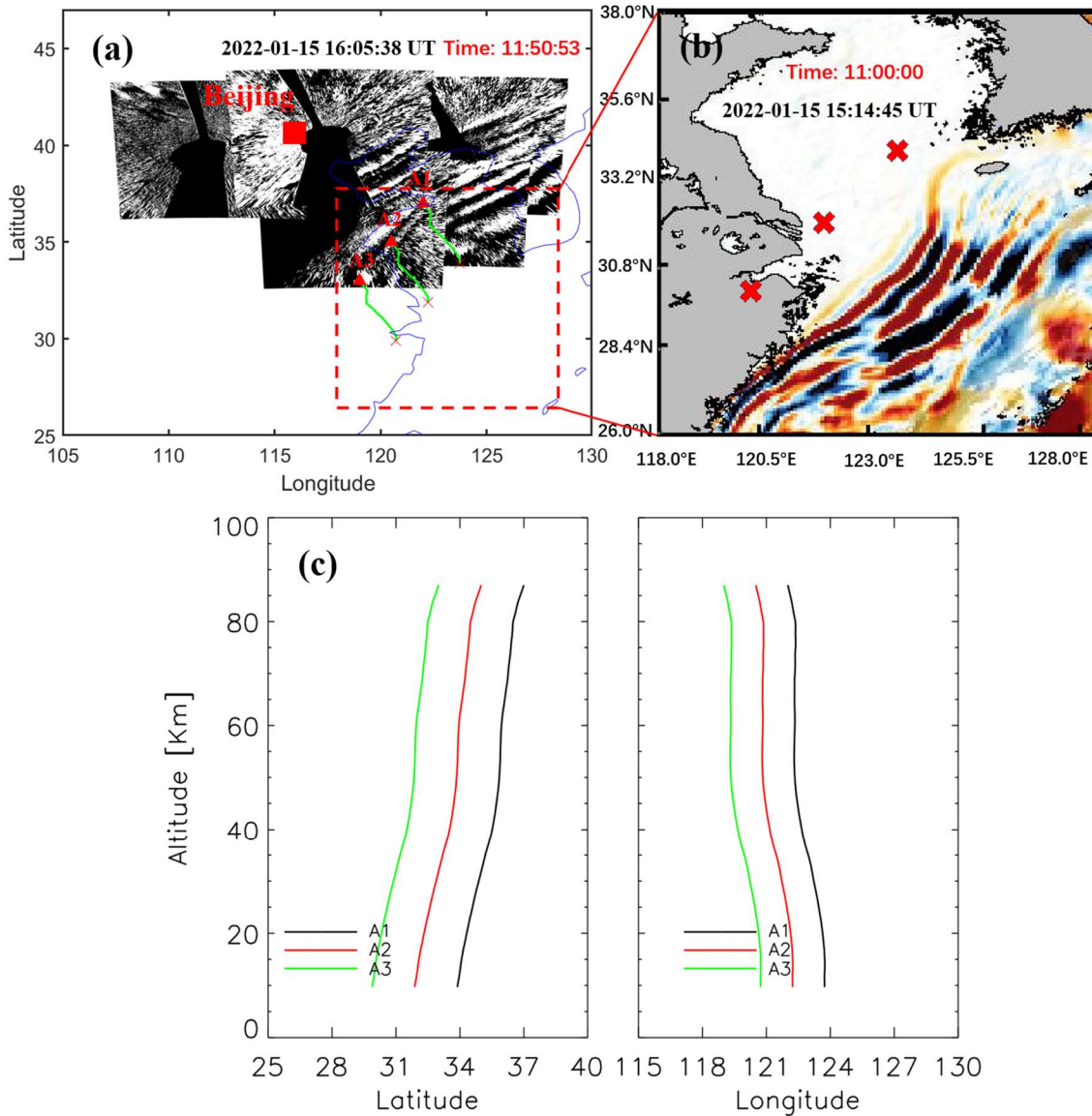
386 Tsunami simulation shows that the surface wave height along the coast of Chinese  
 387 Mainland is in the order of 2 cm. There have been theoretical (Peltier and Hines, 1976) and  
 388 observational (Grave and Makela, 2015, 2017) studies on the relationship between the

389 amplitude of tsunamis and GWs. Peltier and Hines (1976) found that a tsunami amplitude  
 390 of  $\pm 1$  cm at sea level can cause vertical motion of ionospheric E layer and F layer  $\pm 100$  m.  
 391 A more direct observational evidence is that Grawe and Makela (2017) provided airglow  
 392 observation of tsunami-generated ionospheric signatures over Hawaii caused by the 16  
 393 September 2015 Illapel earthquake. They found that vertical disturbances on the sea surface  
 394 not exceeding 2 cm (Fig. 3b of Grawe and Makela, 2017) can create detectable signatures in  
 395 the ionosphere (Fig. 1 of Grawe and Makela, 2017). Therefore, we suggest that the waves  
 396 with larger amplitudes following the leading of TIAPW interact with the atmosphere after  
 397 arriving at the coast of Chinese Mainland to generate the upward propagating AGW packet.



398  
 399 **Figure 10** The background field used for ray tracing analysis for the TIAPW event (a) Saber temperature  
 400 (red) comes from the average temperature of ascending track #1 and descending track #1 in Fig. 9, and  
 401 ERA-5 temperature (black) comes from the average of 15:00 UT and 16:00 UT. (b) Meteor zonal wind  
 402 field (red) and ERA-5 zonal wind field (black). (c) Meteor meridional wind field (red) and ERA-5  
 403 meridional wind field (black). The two red and black lines in (b) and (c) are respectively from 15:00 UT  
 404 and 16:00 UT. The green lines represent the average of two lines. Meteor radar wind field is from  
 405 Beijing station.

406



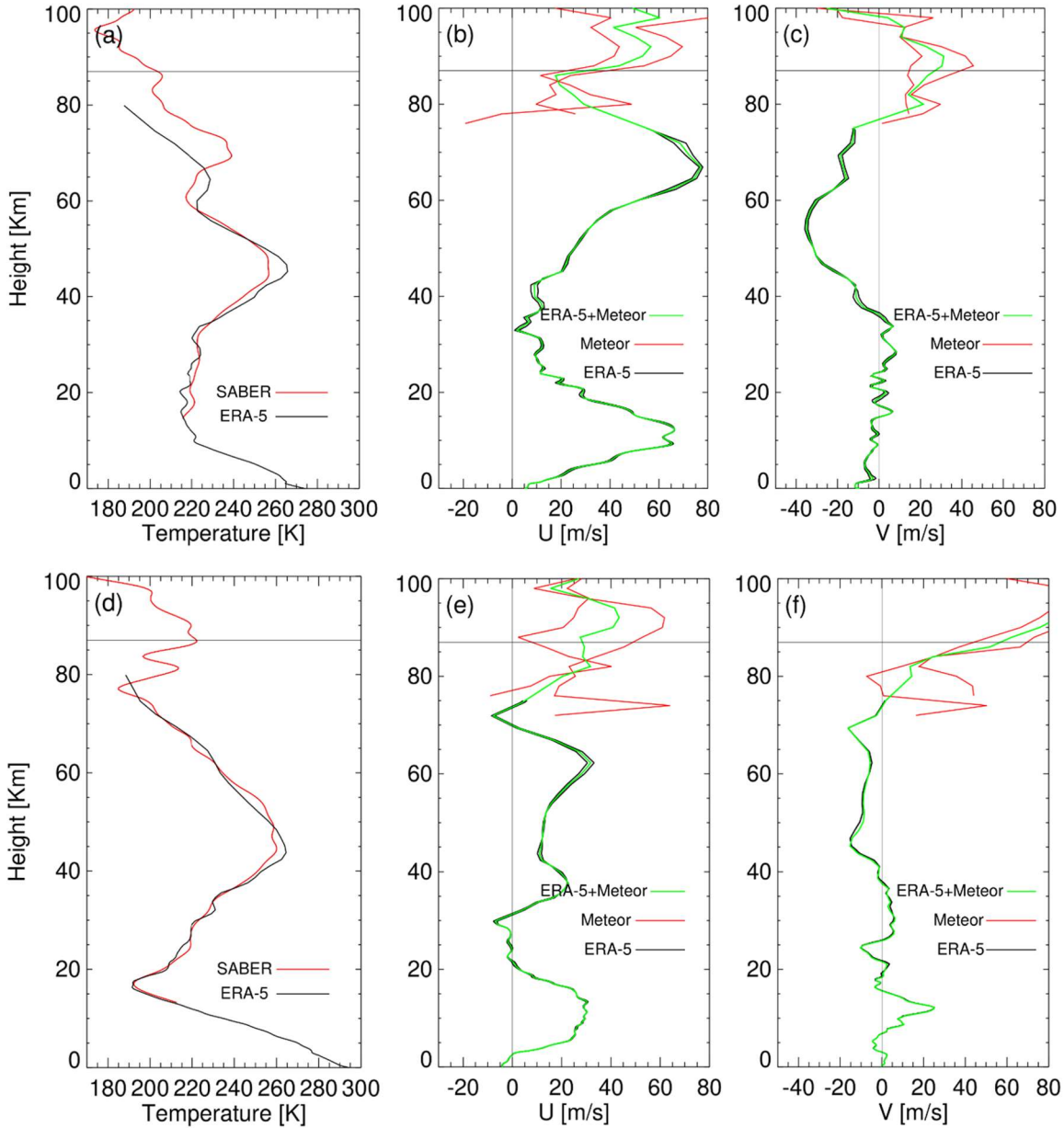
407  
 408 **Figure 11** (a) Backward ray tracing results of the wave packet #3 observed by the OH airglow network.  
 409 The red triangles and red crosses represent the trace start and termination points, respectively. (b)  
 410 Simulated tsunamis induced by the atmospheric pressure wave (TIAPW) corresponding to the dotted  
 411 rectangular area in (a). (c) Ray paths of the wave starting from the seven sampling points in (a).

412 According to the theory of AGW dispersion, the AGW propagating obliquely has  
 413 the following approximate relationship:  $\sin(\varphi) \sim T_b/T$ ,  $\varphi$  is the oblique propagation  
 414 angle,  $T_b$  is the buoyancy period,  $T$  is the intrinsic period. Azeem et al. (2007) found that  
 415 the disturbances in the ionosphere excited by the 2011 Tohoku tsunamis when they reached  
 416 the west coast of the United States. They concluded that the fluctuations observed in TEC  
 417 satisfy AGW dispersion relation, and the period and horizontal wavelength of the TEC

418 disturbances increased with distance from the West Coast of the U.S.

419 From the airglow network observations, we found that the wave packets #4-5 excited  
420 by the tsunamis, continues to propagate over the main land more than 3000 km from the  
421 coast. If the AGWs observed by the airglow network propagate freely rather than being  
422 constrained by duct, we will obtain the propagation characteristics similar to that observed  
423 by Azeem et al. (2007) in the ionosphere from TEC observations.  $T_p$  is about 5min from  
424 the SABER/TIMED observation. The period of wave packet #3 is between 5.5 min and 8.5  
425 min. The minimum propagation angle  $\varphi$  equals  $35^\circ$ , and the corresponding maximum  
426 propagation distance  $L$  is 125 km from  $L \sim H_{oh}/\tan(\varphi)$  estimation, where  $H_{oh}=87$  km is the  
427 height of OH airglow layer. However, our observation does not satisfy the free oblique  
428 propagation dispersion theory of AGWs. In addition, we did not find that the GW  
429 horizontal wavelength increased with the distance from the shore, as predicted by the  
430 theory of AGW oblique propagation. Therefore, the AGWs excited by the tsunami we  
431 observed in the mesopause region may be modulated by duct.

432 We did find a duct structure between 80 and 93 km (black solid line in Fig. 9b), while  
433 the wave packet #3 were in a state of free propagation when they propagate around the  
434 coastal vicinity of Chinese Mainland (dotted line and dashed line). The duct almost includes  
435 the whole OH airglow layer. Therefore, we believe that AGWs generated by TITVE may  
436 enter the duct in the process of propagation over Chinese Mainland. The duct structure over  
437 Chinese Mainland can explain that the GWs generated by the tsunamis can propagate  
438 thousands of kilometers inland.

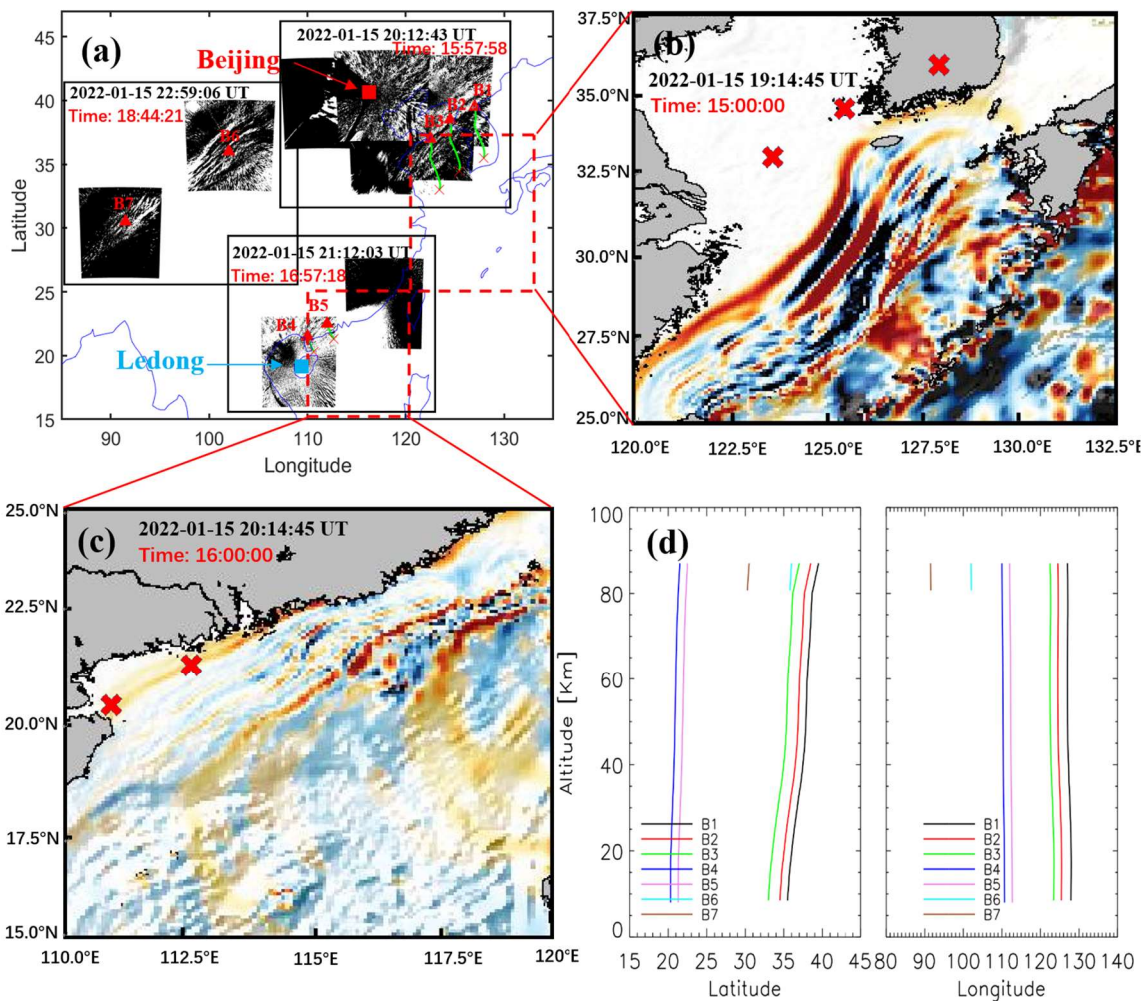


439  
 440 **Figure 12** Similar for Figure 10, but for ray tracing analysis for the TITVE events. The SABER  
 441 temperature field in (a) comes from ascending track #1(21:17:50 UT, 21:18:33UT, 21:19:43 UT, and  
 442 21:20:43 UT) in Fig. 9, and the meteor radar wind fields in (b) and (c) come from Beijing station. The  
 443 SABER temperature field in (d) is from ascending track #1 (21:12:51 UT, 21:14:01 UT, and 21:14:44  
 444 UT) in Fig. 9, and the meteor radar wind fields in (e) and (f) are from Ledong station.  
 445

446 Figure 13 shows the results of ray tracing for wave packets #4-5. The background field  
 447 used for ray tracing analysis for the wave packets #4-5 is from Fig. 12. Meteor radar wind  
 448 field is from Ledong station (18.3°N, 109.4°E). The horizontal wavelength of wave packets  
 449 #4 and #5 observed near the coast by the OH airglow network approximately  $89 \text{ km} \pm 6 \text{ km}$



450 and  $80 \text{ km} \pm 4 \text{ km}$ . We find that the source location of AGWs over the coast of Chinese  
 451 Mainland falls in the near tsunami area, while the location of AGW ray termination over  
 452 the inland is around  $80 \text{ km}$  (position B6 and B7 in Fig. 13d), which indicates that the wave  
 453 meets the evanescent layer (Wrasse et al., 2006). This is consistent with the duct structure  
 454 obtained through dispersion relation. Therefore, we suggest that TITVE interact with the  
 455 atmosphere after arriving at the coast of Chinese Mainland to generate the upward  
 456 propagating AGW packet. After reaching the mesopause region, this wave packet enters the  
 457 wave duct structure in the horizontal propagation process, and this wave duct supports  
 458 wave packet #5 to propagate more than  $3000 \text{ km}$  inland China.



459  
 460 **Figure 13** (a) Backward ray tracing results of the fourth and fifth group GWs observed by the OH airglow

461 network. The red triangles and red crosses represent the trace start and termination points, respectively. (b)  
462 and (c) Simulated tsunami directly induced by the Tonga volcano eruption (TITVE) corresponding to the  
463 dotted rectangular area in (a). (c) Ray paths of the wave starting from the seven sampling points in (a).

#### 464 **4. Conclusions**

465 Strong atmospheric disturbances, including Lamb waves, acoustic waves, and gravity  
466 waves, were triggered by the 2022 HTHH volcano eruption. The HTHH submarine  
467 volcanic eruption also triggered an unusual tsunami, which can generate atmospheric  
468 gravity waves (Fig. 14). We observed five strong group atmospheric waves associated with  
469 the HTHH volcano eruption from the ground-based airglow network observations.

470 The phase speed of the wave packet #1 leading front is approximately 309 m/s, which  
471 is observed almost simultaneously with the surface Lamb wave L0 mode. The  
472 high-frequency wave trains following the wave packet #1 leading front observed by the  
473 northern OH airglow imager network may also be related to the dissipation of the leading  
474 waves. Wave packet #2, with average phase speed of 236 m/s, may be considered as Lamb  
475 wave L1 mode, which exhibits internal GW behavior. Wave packet # 3 and wave packets  
476 #4-5 are generated by TIAPW and TITVE from backward ray tracing analysis. The  
477 horizontal phase speed distribution range of wave packets #3-5 is 200 m/s to 215 m/s,  
478 which is smaller than that of wave packets # 1-2. For amplitude, the average amplitude of  
479 the lamb wave L1 mode (5.4%) is higher than that of the lamb wave L0 mode (3.2%),  
480 while wavepacket # 3, # 4, and # 5 have relatively small amplitudes, mainly distributed  
481 between 0.85% and 1.25%. The horizontal wavelengths of the atmospheric AGWs  
482 observed by the airglow network are very consistent with those of the tsunami near the  
483 coast. This is the first time that we observed the AGWs in the mesopause region triggered

484 by the tsunamis using optical detection equipment. It is also the first time to report  
485 atmospheric gravity waves excited by TIAPW.

486 When the wave excited by TITVE propagate far away from the coast, the  
487 characteristics of AGWs are not consistent with the dispersion of free propagation AGWs.  
488 We find these wave packets are controlled by the duct, which can support the propagation  
489 of these GWs for thousands of kilometers after the tsunami were stopped at the coast.  
490 Therefore, tsunamis can have a significant impact on the upper atmosphere over inland  
491 areas far from the ocean through AGWs.

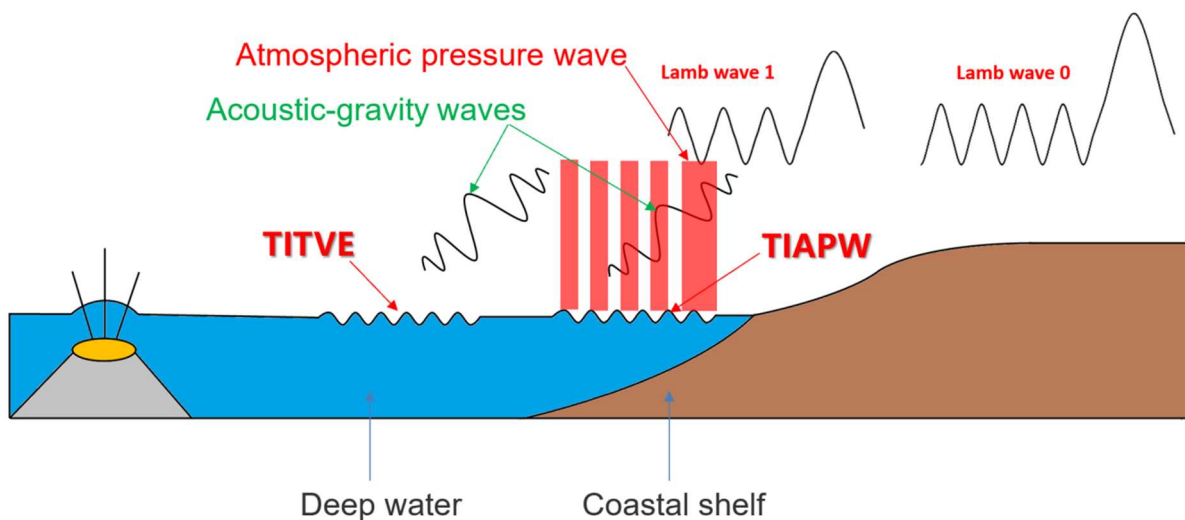
492 The 2022 HTHH volcano eruption form a complex coupling relationship in the land-  
493 ocean-atmosphere system (Fig. 14). Firstly, the heat released by the eruption has a direct  
494 impact on the ocean, causing temperature changes in the surrounding waters. This can lead  
495 to changes in the marine environment, affecting the behavior, distribution, and ecosystem  
496 structure of organisms.

497 Meanwhile, volcanoes release gases such as carbon dioxide and sulfur dioxide.  
498 Carbon dioxide is one of the greenhouse gases that can cause an increase in Earth's  
499 temperature, leading to global warming. Sulfur dioxide can cause sulfuric acid mist in the  
500 atmosphere, which affects the reflectivity and temperature of the atmosphere, and thus  
501 affects the global climate.

502 Moreover, the 2022 HTHH volcano eruptions also trigger atmospheric waves and  
503 tsunamis. The surface atmospheric pressure wave generated by the 2022 HTHH volcano  
504 eruption can affect the upper atmosphere. The conventional tsunami triggered by the Tonga  
505 volcano generated AGWs. The atmospheric pressure wave from the eruption generated a



506 fast tsunami never before observed by tsunami observation networks. When the tsunamis  
 507 reach the coast, their speeds decrease but their amplitudes increase, and the AGWs  
 508 generated by them will also affect the upper atmosphere. These AGWs play an important  
 509 coupling role between the ocean and the atmosphere by affecting the density and pressure  
 510 distribution of the atmosphere during propagation, leading to changes in the wind field and  
 511 affecting global atmospheric circulation. This study exhibits special dynamic coupling  
 512 process between air and sea via acoustic gravity waves (Fig. 14). This indirect impact on  
 513 the upper atmosphere provides a new perspective for us to study the coupling between the  
 514 ocean and the atmosphere and a key opportunity to improve the air-sea coupling model,  
 515 thereby enhancing our future ability to make tsunami warning forecasts.



516  
 517 **Figure 14** The Tonga volcano eruptions triggered two types of tsunamis, one type of tsunami is induced  
 518 by the atmospheric pressure wave (TIAPW) and the other type tsunami is directly induced by the Tonga  
 519 volcano eruption (TITVE). The acoustic gravity waves (AGWs) caused by tsunamis can propagate to the  
 520 mesopause region.  
 521

522 **Data availability**

523 The Multi-Layer Airglow Network data is available  
 524 at <https://data2.meridianproject.ac.cn/data> (MPDC, 2024). TIMED/SABER data is accessed

525 from <http://saber.gats-inc.com/data.php> (last access: 10 January 2024). The ERA5 reanalysis  
526 data are able to be downloaded from the Copernicus Climate Change Service Climate Data  
527 Store through <https://www.ecmwf.int/en/forecasts/datasets/reanalysis-datasets/era5> (last  
528 access: 12 January 2024). Himawari-8 data are distributed by the Center for Environmental  
529 Remote Sensing ([http://www.cr.chiba-u.jp/databases/GEO/H8\\_9/FD/index\\_en\\_V20190123.](http://www.cr.chiba-u.jp/databases/GEO/H8_9/FD/index_en_V20190123.html)  
530 [html](http://www.cr.chiba-u.jp/databases/GEO/H8_9/FD/index_en_V20190123.html)) (last access: 20 January 2024). Meteor data were provided by Beijing National  
531 Observatory of Space Environment, Institute of Geology and Geophysics Chinese  
532 Academy of Sciences through the Geophysics center, National Earth System Science Data  
533 Center (<http://wdc.geophys.ac.cn>) (last access: 15 January 2024).

534

### 535 **Video supplements**

536 Multi-group of strong atmospheric waves observed over China associated with the 2022  
537 Hunga Tonga–Hunga Ha’apai volcano eruptions (<https://doi.org/10.5446/66190> Li, 2024).  
538 Animation series of OH airglow disturbances associated with the 2022 Hunga  
539 Tonga–Hunga Ha’apai volcano eruptions (<https://doi.org/10.5446/s1689> Li, 2024). A strong  
540 wave front observed by an OI 630 nm airglow imager over China associated with the 2022  
541 Hunga Tonga–Hunga Ha’apai volcano eruptions (<https://doi.org/10.5446/66280> Li, 2024).

542

### 543 **Author contributions**

544 J.X and Q.L. conceived the idea of the manuscript. Q.L. carried out the data analysis,  
545 interpretation and manuscript preparation. A.R.G. developed and performed the numerical  
546 simulations. W.L and Y.Z compiled, processed and analysed satellite data. H.L.L., X.L,

547 and W.Y. contributed to the data interpretation and manuscript preparation. All authors  
548 discussed the results and commented on the manuscript.

549

### 550 **Competing interests**

551 The authors declare no competing interests.

552

### 553 **Acknowledgements**

554 This work was supported by the National Science Foundation of China (42374205 and  
555 41974179). The project is also supported by the Specialized Research Fund for State Key  
556 Laboratories. We acknowledge the use of data from the Chinese Meridian Project.

557

### 558 **References**

559 Adam, D.: Tonga volcano eruption created puzzling ripples in Earth's atmosphere, *Nature*,  
560 601, 497, <https://www.nature.com/articles/d41586-022-00127-1>, 2022.

561 Amores, A., Monserrat, S., Marcos, M., Argüeso, D., Villalonga, J., Jordà, G., and Gomis,  
562 D.: Numerical simulation of atmospheric Lamb waves generated by the 2022  
563 Hunga-Tonga volcanic eruption, *Geophysical Research Letters*, 49,  
564 <https://doi.org/10.1029/2022GL098240>, 2022.

565 Astafyeva, E., Maletckii, B., Mikesell, T. D., Munaibari, E., Ravanelli, M., Coisson, P., et al.  
566 The 15 January 2022 Hunga Tonga eruption history as inferred from ionospheric  
567 observations, *Geophysical Research Letters*, 49,  
568 <https://doi.org/10.1029/2022GL098827>, 2022.

569 Azeem, I., Vadas, S. L., Crowley, G., and Makela, J. J.: Traveling ionospheric disturbances

570 over the United States induced by gravity waves from the 2011Tohoku tsunami and  
571 comparison with gravity wave dissipative theory, *J. Geophys. Res. Space Physics*, 122,  
572 3430–3447, <https://doi.org/10.1002/2016JA023659>, 2017.

573 Becker, E. and Vadas, S. L.: Secondary gravity waves in the winter mesosphere: Results from  
574 a high-resolution global circulation model, *Journal of Geophysical Research:*  
575 *Atmospheres*, 123, 2605–2627, <https://doi.org/10.1002/2017JD027460>, 2018.

576 Beer, T. *Atmospheric Waves*, 300 pp., John Wiley, New York, 1974.

577 Carvajal, M., Sepúlveda, I., Gubler, A., and Garreaud, R.: Worldwide signature of the 2022  
578 Tonga volcanic tsunami, *Geophysical Research Letters*, 49(6),  
579 <https://doi.org/10.1029/2022GL098153>, 2022.

580 Donn, W. L., and Balachandran, N. K.: Mount St. Helens eruption of 18 May 1980: Air  
581 waves and explosive yield, *Science* 213, 539 – 541,  
582 <https://doi.org/10.1126/science.213.4507.539>, 1981.

583 Duncombe, J.: The surprising reach of Tonga’s Giant atmospheric waves, *Eos*, 103, 2022.

584 Duncombe, J.: The surprising reach of Tonga’s Giant atmospheric waves, *Eos*, 103,  
585 <https://doi.org/10.1029/2022EO220050>, 2022.

586 Francis, S. H.: Acoustic-gravity modes and large-scale traveling ionospheric disturbances of  
587 a realistic, dissipative atmosphere, *J. Geophys. Res.*, 78 (13), 2278–2301,  
588 <https://doi.org/10.1029/JA078i013p02278>, 1973.

589 Garcia, F. J., Taylor, M. J., and Kelley, M. C.: Two-dimensional spectral analysis of  
590 mesospheric airglow image data, *Appl. Optics*, 36 (29), 7374–7385,  
591 <https://doi.org/10.1364/AO.36.007374>,1997.

592 Ghent, J. N. and Crowell, B. W.: Spectral characteristics of ionospheric disturbances over  
593 the southwestern Pacific from the 15 January 2022 Tonga eruption and tsunami,  
594 Geophysical Research Letters, 49, <https://doi.org/10.1029/2022GL100145>, 2022.

595 Gossard, E. E. and Hooke, W. H.: Waves in the Atmosphere, Elsevier, Amsterdam, 1975,  
596 456.

597 Grawe, M. A. and Makela, J. J.: The ionospheric responses to the 2011 Tohoku, 2012  
598 Haida Gwaii, and 2010 Chile tsunamis: Effects of tsunami orientation and observation  
599 geometry, Earth and Space Science, 2, 472–483,  
600 <https://doi.org/10.1002/2015EA000132>, 2015.

601 Grawe, M. A. and Makela, J. J.: Observation of tsunami-generated ionospheric signatures  
602 over Hawaii caused by the 16 September 2015 Illapel earthquake, J. Geophys. Res.  
603 Space Physics, 122, 1128–1136, <https://doi.org/10.1002/2016JA023228>, 2017.

604 Gusman, A.R., Roger, J., Noble, C. et al. The 2022 Hunga Tonga-Hunga Ha’apai Volcano  
605 Air-Wave Generated Tsunami, Pure and Applied Geophysics, 179, 3511–3525,  
606 <https://doi.org/10.1007/s00024-022-03154-1>, 2022.

607 Harkrider, D. and Press, F.: The Krakatoa air-sea waves: An example of pulse propagation  
608 in coupled systems, Geophys. J. R. Astron. Soc. 13, 149 – 159,  
609 <https://doi.org/10.1111/j.1365-246X.1967.tb02150.x>, 1967.

610 Hersbach, H., Bell, B., Berrisford, P., Hirahara, S., Horányi, A., Muñoz-Sabater, J., Nicolas,  
611 J., Peubey, C., Radu, R., Schepers, D., Simmons, A., Soci, C., Abdalla, S., Abellan, X.,  
612 Balsamo, G., Bechtold, P., Biavati, G., Bidlot, J., Bonavita, M., De Chiara, G.,  
613 Dahlgren, P., Dee, D., Diamantakis, M., Dragani, R., Flemming, J., Forbes, R.,

614 Fuentes, M., Geer, A., Haimberger, L., Healy, S., Hogan, R. J., Hólm, E., Janisková,  
615 M.,Keeley, S., Laloyaux, P., Lopez, P., Lupu, C., Radnoti, G., deRosnay, P., Rozum,  
616 I., Vamborg, F., Villaume, S., and Thépaut, J. N. The ERA5 global reanalysis, *Q. J. R.*  
617 *Meteorol. Soc.*, 146, 1999–2049, <https://doi.org/10.1002/qj.3803>, 2020 (data available  
618 at: <https://www.ecmwf.int/en/forecasts/datasets/reanalysis-datasets/era5> last access: 12  
619 January 2024).

620 Hickey, M. P., Schubert, G., and Walterscheid, R. L.: Propagation of tsunami-driven  
621 gravity waves into the thermosphere and ionosphere, *J. Geophys. Res.*, 114,  
622 <https://doi.org/10.1029/2009JA014105>, 2009.

623 Hickey, M. P., Schubert, G., and Walterscheid, R. L.: Atmospheric airglow fluctuations due  
624 to a tsunami-driven gravity wave disturbance, *Journal of Geophysical Research*,  
625 115(A6), A06308, <https://doi.org/10.1029/2009JA014977>, 2010.

626 Hines, C.: Gravity waves in the atmosphere, *Nature*, 239 (5367), 73–78,  
627 <https://doi.org/10.1038/239073A0>, 1972.

628 Inchin, P. A., Heale, C. J., Snively, J. B., and Zettergren, M. D.: The dynamics of nonlinear  
629 atmospheric acoustic-gravity waves generated by tsunamis over realistic bathymetry,  
630 *Journal of Geophysical Research: Space Physics*, 125,  
631 <https://doi.org/10.1029/2020JA028309>, 2020.

632 Inchin, P. A., Heale, C. J., Snively, J. B., and Zettergren, M.D.: Numerical modeling of  
633 tsunami-generated acoustic-gravity waves in mesopause airglow, *Journal of*  
634 *Geophysical Research: Space Physics*,127, <https://doi.org/10.1029/2022JA030301>,  
635 2022.

636 Koketsu K. and Higashi S.: Three-dimensional topography of the sediment/basement  
637 interface in the Tokyo Metropolitan area, Central Japan, *Bull. seism. Soc. Am.*, 82,  
638 2328-2349, <https://doi.org/10.1785/BSSA0820062328>, 1992.

639 Kubota, T., Saito, T., & Nishida, K.: Global fast-traveling tsunamis driven by atmospheric  
640 Lamb waves on the 2022 Tonga eruption, *Science*, 377, 91-94,  
641 <https://doi.org/10.1126/science.abo4364>, 2022.

642 Laughman, B., Fritts, D. C., and Lund, T. S.: Tsunami-driven gravity waves in the presence  
643 of vertically varying background and tidal wind structures, *J. Geophys. Res. Atmos.*,  
644 122, 5076-5096, <https://doi.org/10.1002/2016JD025673>, 2017.

645 Li, X., Ding, F., Yue, X., Mao, T., Xiong, B., and Song, Q.: Multiwave structure of  
646 traveling ionospheric disturbances excited by the Tonga volcanic eruptions observed  
647 by a dense GNSS network in China, *Space Weather*, 21,  
648 <https://doi.org/10.1029/2022SW003210>, 2023.

649 Lighthill, M. J.: *Waves in Fluids*, Cambridge University Press, Cambridge, UK, New York,  
650 504 pp., ISBN: 0-521-01045-4, 1978.

651 Lin, J.-T., Rajesh, P. K., Lin, C. C. H., Chou, M.-Y., Liu, J.-Y., Yue, J., et al. Rapid  
652 conjugate appearance of the giant ionospheric Lamb wave signatures in the northern  
653 hemisphere after Hunga-Tonga volcano eruptions, *Geophysical Research Letters*, 49,  
654 <https://doi.org/10.1029/2022GL098222>, 2022.

655 Lindzen, R. S. and Blake, D.: Lamb waves in the presence of realistic distributions of  
656 temperature and dissipation, *Journal of Geophysical Research*, 77(12), 2166 – 2176,  
657 <https://doi.org/10.1029/JC077i012p02166>, 1972.

658 Li, Q., Xu, J., Liu, H., Liu, X., and Yuan, W.: How do gravity waves triggered by a typhoon  
659 propagate from the troposphere to the upper atmosphere?. *Atmos. Chem. Phys.*, 22,  
660 12077–12091, <https://doi.org/10.5194/acp-22-12077-2022>, 2022.

661 Li, Q.: Multi-group of strong atmospheric waves observed over China associated with the  
662 2022 Hunga Tonga–Hunga Ha’apai volcano eruptions, TIB AV-Portal [video],  
663 <https://doi.org/10.5446/66190>, 2024.

664 Li, Q.: Animation series of OH airglow disturbances associated with the 2022 Hunga  
665 Tonga–Hunga Ha’apai volcano eruptions, TIB AV-Portal [video],  
666 [https://doi.org/10.5446/s\\_1689](https://doi.org/10.5446/s_1689), 2024. Li, Q.: A strong wave front observed by an OI 630  
667 nm airglow imager over China associated with the 2022 Hunga Tonga–Hunga Ha’apai  
668 volcano eruptions, TIB AV-Portal [video], <https://doi.org/10.5446/66280>, 2024.

669 Liu, H.-L., Wang, W., Huba, J.D., Lauritzen, P. H., and Vitt, F. Atmospheric and  
670 Ionospheric Responses to Hunga-Tonga Volcano Eruption Simulated by WACCM-X,  
671 *Geophysical Research Letters*, 50, <https://doi.org/10.1029/2023GL103682>, 2023.

672 Liu, X., Xu, J., Yue, J., and Kogure, M.: Strong gravity waves associated with Tonga  
673 volcano eruption revealed by SABER observations, *Geophysical Research Letters*, 49,  
674 <https://doi.org/10.1029/2022GL098339>, 2022.

675 Makela, J. J., Lognonné, P., Hébert, H., Gehrels, T., Rolland, L., Allgeyer, S., et al. Imaging  
676 and modeling the ionospheric airglow response over Hawaii to the tsunami generated by  
677 the Tohoku earthquake of 11 March 2011, *Geophysical Research Letters*, 38 (24),  
678 <https://doi.org/10.1029/2011GL047860>, 2011.

679 MPDC: Airglow data [data set], <https://data2.meridianproject.ac.cn/data>, last access: 15



680 January 2024.

681 Nishikawa, Y., Yamamoto, My., Nakajima, K. et al. Observation and simulation of  
682 atmospheric gravity waves exciting subsequent tsunami along the coastline of Japan  
683 after Tonga explosion event, *Sci Rep* 12, 22354, <https://doi.org/10.1038/s41598-022-25854-3>, 2022.

685 Occhipinti, G., Rolland, L., Lognonné, P., and Watada, S.: From Sumatra 2004 to  
686 Tohoku-Oki 2011: The systematic GPS detection of the ionospheric signature induced  
687 by tsunamigenic earthquakes, *Journal of Geophysical Research: Space Physics*, 118,  
688 3626–3636, <https://doi.org/10.1002/jgra.50322>, 2013.

689 Omira, R., Ramalho, R.S., Kim, J. et al. Global Tonga tsunami explained by a fast-moving  
690 atmospheric source, *Nature* 609, 734–740, <https://doi.org/10.1038/s41586-022-04926-4>, 2022.

692 Otsuka, S.: Visualizing Lamb waves from a volcanic eruption using meteorological satellite  
693 Himawari-8. *Geophysical Research Letters*, 49, <https://doi.org/10.1029/2022GL098324>, 2022 (data available at: [http://www.cr.chiba-u.jp/databases/GEO/H8\\_9/FD/index\\_en\\_V20190123.html](http://www.cr.chiba-u.jp/databases/GEO/H8_9/FD/index_en_V20190123.html) last access: 20 January 2024).

696 Peltier, W., and Hines, C.: On the possible detection of tsunamis by a monitoring of the  
697 ionosphere, *Journal of Geophysical Research*, 81(12), 1995–2000,  
698 <https://doi.org/10.1029/JC081i012p01995>, 1976.

699 Poblet, F. L., Chau, J. L., Conte, J. F., Vierinen, J., Suclupe, J., Liu, A., and Rodriguez, R. R.:  
700 Extreme horizontal wind perturbations in the mesosphere and lower thermosphere over  
701 South America associated with the 2022 Hunga eruption, *Geophysical Research Letters*,

702 50, <https://doi.org/10.1029/2023GL103809>, 2023.

703 Pradipta, R., Carter, B. A., Currie, J. L., Choy, S., Wilkinson, P., Maher, P., and Marshall, R.:  
704 On the propagation of traveling ionospheric disturbances from the Hunga Tonga-Hunga  
705 Ha'apai volcano eruption and their possible connection with tsunami waves,  
706 *Geophysical Research Letters*, 50, <https://doi.org/10.1029/2022GL101925>, 2023.

707 Press, F. and Harkrider, D. G.: "Propagation of acoustic-gravity waves in the atmosphere," *J.*  
708 *Geophys. Res.* 67, 3889–3908, 1962.[doi:10.1029/JZ067i010p03889](https://doi.org/10.1029/JZ067i010p03889).

709 Salmon, R.: *Introduction to ocean waves*, Scripps Inst. of Oceanogr., Univ. of Calif., San  
710 Diego., 2014.

711 Sepúlveda, I., Carvajal, M., and Agnew, D. C.: Global winds shape planetary-scale Lamb  
712 waves. *Geophysical Research Letters*, 50, <https://doi.org/10.1029/2023GL106097>,  
713 2023

714 Smith, S. M., Martinis, C. R., Baumgardner, J., and Mendillo, M.: All-sky imaging of  
715 transglobal thermospheric gravity waves generated by the March 2011 Tohoku  
716 Earthquake, *J. Geophys. Res. Space Physics*, 120, 10,992–10,999,  
717 <https://doi.org/10.1002/2015JA021638>, 2015.

718 Stober, G., Liu, A., Kozlovsky, A., Qiao, Z., Krochin, W., Shi, G., Kero, J., Tsutsumi, M.,  
719 Gulbrandsen, N., Nozawa, S., Lester, M., Baumgarten, K., Belova, E., and Mitchell, N.:  
720 Identifying gravity waves launched by the Hunga Tonga–Hunga Ha'apai volcanic  
721 eruption in mesosphere/lower-thermosphere winds derived from CONDOR and the  
722 Nordic Meteor Radar Cluster, *Ann. Geophys.*, 41, 197–208,  
723 <https://doi.org/10.5194/angeo-41-197-2023>, 2023.

724 Stober, G., Vadas, S. L., Becker, E., Liu, A., Kozlovsky, A., Janches, D., Qiao, Z., Krochin,  
725 W., Shi, G., Yi, W., Zeng, J., Brown, P., Vida, D., Hindley, N., Jacobi, C., Murphy, D.,  
726 Buriti, R., Andrioli, V., Batista, P., Marino, J., Palo, S., Thorsen, D., Tsutsumi, M.,  
727 Gulbrandsen, N., Nozawa, S., Lester, M., Baumgarten, K., Kero, J., Belova, E., Mitchell,  
728 N., Moffat-Griffin, T., and Li, N.: Gravity waves generated by the Hunga Tonga–Hunga  
729 Ha’apai volcanic eruption and their global propagation in the mesosphere/lower  
730 thermosphere observed by meteor radars and modeled with the High-Altitude general  
731 Mechanistic Circulation Model, *Atmos. Chem. Phys.*, 24, 4851–4873,  
732 <https://doi.org/10.5194/acp-24-4851-2024>, 2024.

733 Swenson, G. R. and Mende, S. B.: OH emission and gravity waves (including a breaking  
734 wave) in all-sky imagery from Bear Lake, UT, *Geophys. Res. Lett.*, 21, 2239–2242,  
735 <https://doi.org/10.1029/94GL02112>, 1994.

736 Symons, G. J.: *The Eruption of Krakatoa, and Subsequent Phenomena: Report of the*  
737 *Krakatoa Committee of the Royal Society (Wiley Online Library)*, 1888.

738 Takahashi, H., Figueiredo, C.A.O.B., Barros, D. et al. Ionospheric disturbances over South  
739 America related to Tonga volcanic eruption, *Earth Planets Space* 75, 92,  
740 <https://doi.org/10.1186/s40623-023-01844-1>, 2023.

741 Tang, J., Kamalabadi, F., Franke, S. J., Liu, A. Z., and Swenson, G. R.: Estimation of gravity  
742 wave momentum flux with spectroscopic imaging, *IEEE T. Geosci. Remote*, 43,  
743 103–109, <https://doi.org/10.1109/TGRS.2004.836268>, 2005.

744 Themens, D. R., Watson, C., Zagar, N., Vasylykevych, S., Elvidge, S., McCaffrey, A., et al.  
745 Global propagation of ionospheric disturbances associated with the 2022 Tonga

746 volcanic eruption, *Geophysical Research Letters*, 49(7),  
747 <https://doi.org/10.1029/2022GL098158>, 2022.

748 Vadas, S. L., Becker, E., Figueiredo, C., Bossert, K., Harding, B. J., and Gasque, L. C.:  
749 Primary and secondary gravity waves and large-scale wind changes generated by the  
750 Tonga volcanic eruption on 15 January 2022: Modeling and comparison with  
751 ICON-MIGHTI winds, *Journal of Geophysical Research: Space Physics*, 128,  
752 <https://doi.org/10.1029/2022JA031138>, 2023.

753 Vadas, S. L. and Becker, E.: Numerical modeling of the excitation, propagation, and  
754 dissipation of primary and secondary gravity waves during wintertime at McMurdo  
755 Station in the Antarctic, *Journal of Geophysical Research: Atmospheres*, 123,  
756 9326–9369, <https://doi.org/10.1029/2017JD027974>, 2018.

757 Vadas, S. L., Makela, J. J., Nicolls, M. J., and Milliff, R. F.: Excitation of gravity waves by  
758 ocean surface wave packets: Upward propagation and reconstruction of the  
759 thermospheric gravity wave field, *J. Geophys. Res. Space Physics*, 120, 9748–9780,  
760 <https://doi.org/10.1002/2015JA021430>, 2015.

761 Vadas, S. L., Zhao, J., Chu, X., and Becker, E.: The excitation of secondary gravity waves  
762 from local body forces: Theory and observation, *Journal of Geophysical Research:*  
763 *Atmospheres*, 123, 9296–9325, <https://doi.org/10.1029/2017JD027970>, 2018.

764 Xu, J., Li, Q., Sun, L., Liu, X., Yuan, W., Wang, W., Yue, J., Zhang, S., Liu, W., Jiang, G.,  
765 Wu, K., Gao, H., and Lai, C.: The Ground - Based Airglow Imager Network in China:  
766 Recent Observational Results, *Geophysical Monograph Series*, 261, 365-394,  
767 <https://doi.org/10.1002/9781119815631.ch19>, 2021.

768 Xu, J., et al. Concentric gravity waves over northern China observed by an airglow imager  
769 network and satellites, *J. Geophys. Res. Atmos.*, 120, 11,058–11,078,  
770 <https://doi.org/10.1002/2015JD023786>, 2015.

771 Yamada, M., Ho, T.-C., Mori, J., Nishikawa, Y., and Yamamoto, M.-Y.: Tsunami triggered  
772 by the Lamb wave from the 2022 Tonga volcanic eruption and transition in the  
773 offshore Japan region, *Geophysical Research Letters*, 49,  
774 <https://doi.org/10.1029/2022GL098752>, 2022.

775 Yeh, K. C. and Liu, C. H.: Acoustic-Gravity Waves in the Upper Atmosphere, *Reviews of*  
776 *Geophysics and Space Physics*, 12 (2), 193, <https://doi.org/10.1029/RG012i002p00193>,  
777 1974.

778 Wrasse, C. M., Nakamura, T., Tsuda, T., Takahashi, H., Medeiros, A. F., Taylor, M.  
779 J., Gobbi, D., Salatun, A., Suratno, E. A., and Admiranto, A. G.: Reverse ray tracing of  
780 the mesospheric gravity waves observed at 23°S (Brazil) and 7°S (Indonesia) in airglow  
781 imagers, *J. Atmos. Sol. Terr. Phys.*, 68, 163– 181,  
782 <https://doi.org/10.1016/j.jastp.2005.10.012>, 2006.

783 Wright, C. J., et al. Surface-to-space atmospheric waves from Hunga Tonga-Hunga Ha’apai  
784 eruption, *Nature*, 609 (7928), 741–746, <https://doi.org/10.1038/s41586-022-05012-5>,  
785 2022.

786 Zhang, S., Vierinen, J., Aa, E., Goncharenko, L. P., Erickson, P., Rideout, W., et al. 2022  
787 Tonga volcanic eruption induced global propagation of ionospheric disturbances via  
788 Lamb waves, *Frontiers in Astronomy and Space Sciences*, 9, 1–10,  
789 <https://doi.org/10.3389/fspas.2022.871275>, 2022.